Journal Pre-proof

Locally Sourced Multifunctional LC^3–Biochar Composite for 3D Printed Construction: Mechanical Performance, Self-Sensing Behaviour, and CO_2-Uptake Capability

Abedi Mohammadmahdi, Waris Muhammad Bilal, Al-Alawi Mubarak, Al-Jabri Khalifa

PII: S2238-7854(26)01137-3

DOI: https://doi.org/10.1016/j.jmrt.2026.05.084

Reference: JMRTEC 17228

To appear in: *Journal of Materials Research and Technology*

Received Date: 19 February 2026

Revised Date: 27 April 2026

Accepted Date: 8 May 2026

Please cite this article as: Abedi M, Waris MB, Al-Alawi M, Al-Jabri K, Locally Sourced Multifunctional LC^3–Biochar Composite for 3D Printed Construction: Mechanical Performance, Self-Sensing Behaviour, and CO_2-Uptake Capability, *Journal of Materials Research and Technology*, https://doi.org/10.1016/j.jmrt.2026.05.084.

Locally Sourced Multifunctional LC³–Biochar Composite for 3D Printed Construction: Mechanical Performance, Self-Sensing Behaviour, and CO_2-Uptake Capability

Abstract

Most conductive multifunctional cementitious composites rely on synthetic carbon-based additives with high embodied carbon, and rarely integrate both self-sensing and CO_2-capture functionalities within a single system. This study develops a multifunctional eco-friendly 3D-printed LC³–biochar composite using natural and locally sourced Omani materials, combining adequate mechanical performance, self-sensing capability, and CO_2-uptake functionality. The binder replaces 40% of OPC with limestone–calcined clay, while mixtures incorporate 4.25 wt.% biochar and 0–1.6 vol.% goat-hair fibres to tailor conductivity, rheology, and printability. An optimal fibre content of 0.8% was identified, balancing workability, microstructural stability, and electromechanical responsiveness. Rheological behaviour, mechanical performance (in printing-induced directions), durability under elevated temperature and acid–chloride exposure, and cyclic electromechanical sensing (at 30% and 60% compressive strength) were evaluated. Self-sensing was quantified via fractional resistance change, while machine-learning models predicted stress, strain, modulus, and a damage index. Microstructural analyses (SEM, TGA/DTG, MIP) confirmed pore structure and fibre–matrix interactions. The composites achieved compressive strength up to 34 MPa and flexural strength up to 4.8 MPa (perpendicular) and 3.6 MPa (parallel), with good durability (76–79% strength retention at 300 °C and 38–52% at 500 °C). Stable sensing responses (5–13% FCR) and reliable ML-based degradation tracking were obtained. CO_2 uptake reached ~1000 g/m² in Cycle 1 and stabilised after regeneration, with behaviour validated via coupled mass–resistivity analysis. Additionally, embodied carbon was reduced by ~25% compared to OPC. These results demonstrate the potential of LC³–biochar composites as a sustainable platform for next-generation smart and low-carbon digital construction.

Keywords: 3D Printed Construction; Limestone–Calcined Clay (LC³); Biochar; Natural Animal-Hair Fibre; Self-Sensing; CO_2 Uptake.

1. Introduction

1.1. Background

Advances in 3D concrete printing (3DCP) have positioned digital fabrication as a transformative pillar in the construction sector, supporting the EU Vision 2030 priorities of industrialised automation, productivity enhancement, material circularity, and reduced environmental impact [1,2]. Through automated layer-wise deposition, 3DCP enables geometric freedom, minimises labour dependency, reduces construction waste by 30–60%, and increases production efficiency by up to two- to three-fold [3]. Yet printable mortars intrinsically demand high cement contents because buildability, early structural rigidity, and interlayer stability must be achieved in the absence of large aggregates and without conventional steel reinforcement—forcing the binder to compensate for mechanical and rheological requirements [4]. Given that global cement production exceeds 4.1 billion tonnes annually and contributes 7–8% of anthropogenic CO_2 emissions, this dependency is increasingly incompatible with the sector's mandated decarbonisation trajectories [2,5]. In this context, Limestone–Calcined Clay Cement (LC³) has emerged as a highly scalable low-carbon binder, wherein 35–50% clinker replacement yields 35–45% reductions in CO_2 emissions while improving key engineering parameters [6]. Importantly, natural clay deposits worldwide are dominantly composed of kaolinite, illite, and montmorillonite, whereas other clay minerals occur at much lower abundances and typically have negligible influence on mechanical or rheological performance

[2,4,5]. LC³ therefore leverages precisely these abundant clay types, enabling direct use of naturally occurring kaolinitic–illitic–montmorillonitic resources without requiring high-purity beneficiation, and eliminating the energy-intensive metakaolin purification chain [3]. Across the 35–50% substitution range, LC³ enhances early hydration kinetics, increases packing density, refines pore structure, and often improves long-term mechanical strength and durability (chloride, acid, and thermal resistance) by 5–20% [2].

Recent studies have expanded LC³ applications beyond conventional concrete. Khan et al. [7] developed LC³-based concrete incorporating geopolymer cold-bonded artificial aggregates and achieved high compressive strength (~71 MPa) with ~57% reduction in global warming potential, demonstrating the potential of LC³ in advanced sustainable composite systems. Similarly, Khedkar et al. [8] investigated LC³ concrete with recycled rubber aggregates and reported acceptable mechanical performance at optimal replacement levels (~10%) for the modern digital construction, highlighting its capability for waste-integrated structural applications. Abedi et al.[5] developed a multifunctional LC³-based 3D-printed composite incorporating recycled carbon nanotubes (CNTs) to enable both self-sensing and self-heating capabilities. The results showed that the optimized composite achieved a compressive strength of about 35 MPa along with stable piezoresistive responses under cyclic loading, demonstrating its effectiveness for structural health monitoring. However, despite these advantages, CNTs remain expensive and energy-intensive materials, and their production is associated with a relatively high carbon footprint, which limits their sustainability in low-carbon construction applications. These studies indicate that LC³ is increasingly being adopted in modern material design [9–11]. Although LC³ is inherently a low-carbon binder, the development of low-carbon, multifunctional LC³-based systems for advanced construction technologies such as 3D printing has not yet been realized.

Fibre reinforcement has been increasingly incorporated into 3DPC systems to compensate for the absence of coarse aggregates and continuous steel reinforcement, with both synthetic and natural fibres being employed to enhance tensile capacity, interlayer cohesion, and crack-control efficiency [12]. In extrusion-based 3DCP, synthetic fibres such as polypropylene (0.3–1.0 vol%, length 6–12 mm, diameter 18–40 μm), PVA (0.5–1.5 vol%, length 6–12 mm), glass microfibres (0.5–2.0 vol%, length 3–13 mm), and basalt fibres (0.2–0.6 vol%, length 6–20 mm) have been shown by Nematollahi et al.[13], Ramezani et al.[14], Varela et al.[15], and Sun et al.[16] to improve buildability, reduce edge cracking, and increase flexural resistance. In LC³-based printable composites, Li et al.[17] demonstrated that fibre addition enhances filament integrity and post-cracking ductility. Similar strategies have been adopted in conventional cement mortars using steel, carbon, cellulose, and hybrid fibres to improve toughness and shrinkage resistance, as noted by Ramezani et al.[14]. Natural fibres, however, present unique sustainability and functional advantages [18]. Widely studied plant-based fibres—such as sisal (length 10–50 mm, diameter 50–200 μm), jute (10–40 mm, 20–100 μm), hemp (10–30 mm, 25–80 μm), coir (10–30 mm, 100–300 μm), and flax (10–60 mm, 15–80 μm)—provide biodegradability, low density, and strong crack-bridging capacity, although their hydrophilicity can affect long-term stability [18][19]. Synthetic fibres—even recycled ones—persist for decades in the environment and fragment into microplastics [18]. In contrast, animal-hair fibres such as

goat hair, sheep wool, horsehair, and camel hair typically possess lengths of 6–15 mm and diameters of 20–80 μm, with a keratin-based microstructure and overlapping cuticle scales that promote mechanical interlocking, excellent dispersibility, high flexibility, and elongation-at-break of 20–40% [20–23]. However, to the best of current knowledge, the use of natural animal-hair fibres such as goat hair in 3D-printed LC³ composites is scarcely reported and remains largely unexplored in the existing literature.

Structural health monitoring is particularly critical in 3DPC due to the process inherently produces anisotropic, layer-dependent architectures with interfaces that may act as preferential damage paths, while the absence of conventional reinforcement further increases the need for continuous condition assessment [5]. Traditional systems not only rely on externally mounted sensors that are costly, difficult to integrate, and mechanically incompatible with cementitious substrates, but also require a large number of sensors to achieve high-resolution monitoring, making deployment complex and unsustainable [24]. Piezoresistive self-sensing materials overcome these limitations by converting the cementitious matrix itself into a distributed sensor [25]. This is achieved by introducing conductive phases—such as carbon black at 0.5–2 wt%, which increases viscosity yet enhances crack resistance and provides a gauge factor typically between 20 and 80 (i.e., the ratio between fractional resistance change and strain); graphite at 1–10 wt% with stable conductivity and gauge factors around 40–120; CNTs at 0.05–0.5 wt% [26], which strengthen the matrix and yield gauge factors near 100–200; and graphene nanoplatelets at 0.1–1.0 wt%, which refine pore structure and exhibit gauge factors of roughly 80–180—added near their percolation threshold where conduction arises from particle contacts and tunneling effects [26,27]. Mechanical loading modulates inter-particle spacing within this network, producing reversible changes in bulk resistivity that directly track strain and microcrack evolution [25,28]. Among conductive additives, biochar, a porous carbonaceous product of biomass pyrolysis, forms highly stable conductive paths; when incorporated at 1–10 wt%, it enhances conductivity [29], moderately increases yield stress without impairing pumpability [30], improves crack-bridging sensitivity [31], and typically demonstrates gauge factors in the range of 50–150 [29,32]. Its renewability, high surface area, and low embodied energy make biochar a sustainable and efficient alternative to synthetic nanocarbons for self-sensing 3D-printed LC³ composites. Biochar also contributes to CO_2 mitigation through physical adsorption in its micro–mesoporous network and limited chemisorptive interactions linked to alkaline functional groups [33,34]. Its hierarchical pore system enables van der Waals-based uptake, capillary trapping, and partial carbonation when incorporated into cementitious matrices [33]. Dosages of 1–10 wt% biochar in cementitious composites typically yield CO_2 sequestration capacities of 20–80 mg CO_2 per gram of biochar, resulting in 1–3% uptake relative to binder mass depending on surface area and pyrolysis conditions [35,36]. Liu et al.[37] developed biochar-incorporated red-mud-based artificial lightweight aggregates and reported enhanced CO_2 sequestration of ~30–33 kg/t, attributed to the synergistic effect of biochar porosity and alkaline phases facilitating carbonation. In a related study, Liu et al.[38] also demonstrated that waste-based cold-bonded aggregates (CSW-ALCBAs) can achieve up to ~0.20 g/g CO_2 uptake through accelerated carbonation, highlighting the role of porous matrices in promoting CO_2 diffusion and fixation. Furthermore, recent studies have

shown that biochar-modified cementitious systems enhance CO_2 adsorption through combined pore-driven physical trapping and mineral carbonation mechanisms. These carbon-capture capabilities, combined with biochar's conductive behavior and stable dispersion, reinforce its role as a multifunctional additive for sustainable, self-sensing LC³-based 3D-printed composites. However, to date, the integration of biochar for individual or combined self-sensing functionality and CO_2-capture performance in 3D-printed LC³ systems has not yet been systematically investigated.

1.2. Objectives of the Study

Following the knowledge gaps identified in the literature survey, the novelty of this research is to develop a resource-efficient eco-friendly multifunctional 3D-printed LC³ composite combining proper mechanical performance, intrinsic self-sensing capability, and CO_2-intake behaviour using natural, sustainable, and locally sourced constituents, including animal-hair fibres and biochar. This direction gains importance given Oman's high overall cement consumption—estimated at several million tonnes annually—and the labour-intensive nature of conventional construction, which make digitally fabricated LC³ systems economically and environmentally advantageous [2,5]. Oman hosts extensive clay and limestone deposits in regions such as Al-Sharqiyah, Al-Dakhiliyah, Dhofar, and Al-Batinah, amounting to tens of millions of tonnes and enabling low-embodied-energy LC³ production at reduced cost [3,4]. Substantial quantities of animal hair from goats, sheep, and camels are routinely discarded despite their potential as renewable reinforcement [39], while agricultural residues—especially date-palm waste—offer a viable source for producing biochar [40]. In Oman's hot, arid climate, where elevated CO_2 concentrations in enclosed spaces pose environmental and health concerns [41], a material capable of both structural performance and CO_2 intake becomes particularly relevant. The resulting composite links advanced digital fabrication with a material system inherently aligned with Oman's climate, resource base, and architectural culture, creating a locally grounded yet technologically modern construction solution. Accordingly, the objectives of this study are defined as follows:

I. To investigate the influence of natural animal-hair fibres on the mechanical, rheological, microstructural, and durability behaviour of 3D-printed LC³ composites.

II. To evaluate the effect of biochar on the mechanical, rheological, microstructural, and durability performance of 3D-printed LC³ composites.

III. To develop a piezoresistive self-sensing biochar-based 3D-printed LC³ composite capable of detecting stress, strain, and damage index through integrated experimental testing and machine-learning models.

IV. To assess the CO_2-intake performance of biochar-modified 3D-printed LC³ composites and benchmark it against other carbon-capture construction materials.

2. Materials and Methods

2.1. Raw materials.

The cementitious binder used in this study was formulated through a combination of OPC (CEM I 42.5 R), a limestone–calcined clay blend, and a fine siliceous aggregate. The OPC complied with EN 197-1, and its chemical/physical characteristics are provided in Table 1. The calcined clays—kaolinite, illite, and sodium-montmorillonite—were sourced in pre-calcined form from United Engineering Services Co. LLC (Oman) and subsequently processed to ensure consistent fineness and reactivity (Figure 1). Their mineralogical profiles, determined through X-ray Diffraction (XRD) and X-ray Fluorescence (XRF), are illustrated in Figure 2 and Table 2.

The thermal activation of the montmorillonite resulted in a broad hump centered near 21.50° 2θ, reflecting partial amorphization associated with dehydroxylation [42]. The kaolinite-derived metakaolin phase displayed a distinct peak around 22.13° 2θ, confirming the successful transformation to a highly reactive amorphous aluminosilicate [43]. In contrast, the illite fraction retained a pronounced reflection near 22.31° 2θ, consistent with its well-known thermal stability and limited structural breakdown during calcination [44]. To ensure uniform dispersion within the binder matrix, all calcined clays and the supplementary limestone were dry-milled and sieved through a 45 μm screen (No. 325), resulting in a median particle size (D_{50}) of approximately 12 ± 2 μm, consistent with recommended fineness levels for pozzolanic reactivity enhancement [45].

Table 1. Chemical composition and initial setting time of the OPC (CEM I 42.5 R) used in this study.

SiO_2 (%)	Al_2O_3 (%)	Fe_2O_3 (%)	MgO (%)	CaO (%)	Na_2O (%)	TiO_2 (%)	K_2O (%)	MnO (%)	P_2O_5 (%)	SO_3 (%)	LOI[a] (%)	Initial setting time (min)[b]
19.90	4.70	3.38	1.30	63.93	0.17	0.24	0.44	0.079	0.063	2.54	2.97	194

[a] (Loss on ignition) EN 196-2, [b] EN 196-3.

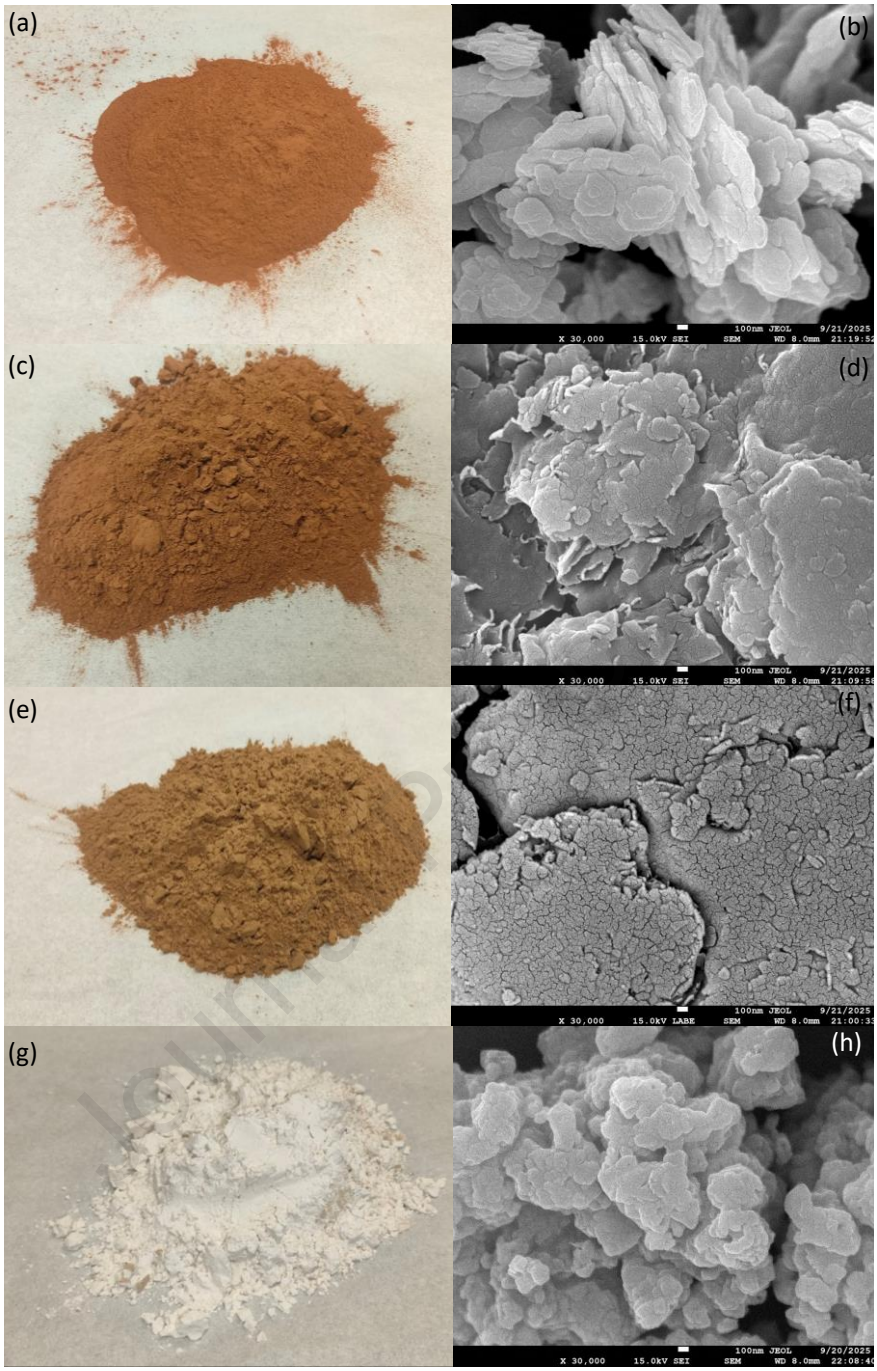

Figure 1. Macroscopic appearance and SEM microstructural features of the calcined clay components and limestone used in the LC³ system: (a, b) kaolinite showing thermally activated plate-like metakaolin layers; (c, d) illite exhibiting partially collapsed aluminosilicate sheets following calcination; (e, f) sodium-based montmorillonite displaying aggregated, dehydroxylated structures with reduced basal spacing; and (g, h) finely ground limestone presenting dense, angular carbonate particles.

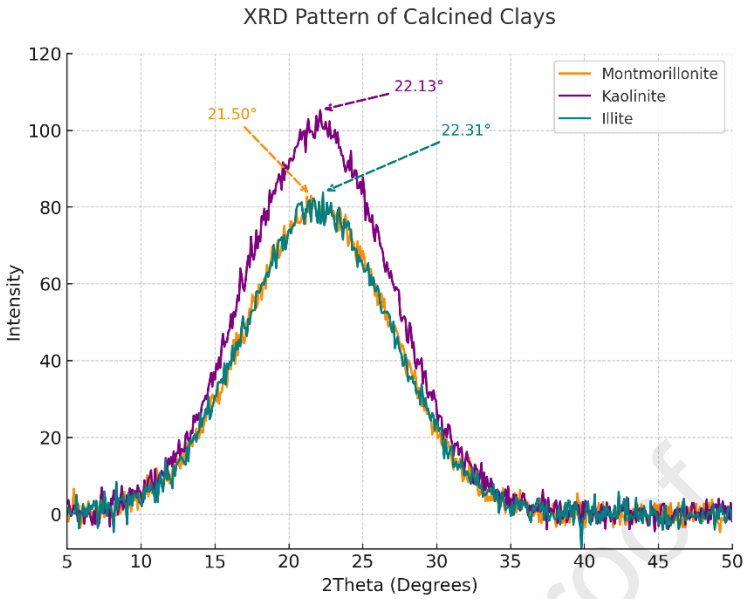

Figure 2. (XRD) patterns of the calcined clay components used in the LC³ system.

Table 2. Oxide composition (wt%) of the raw solid constituents used in this study, including calcined kaolinite, illite, montmorillonite, and ground limestone.

Material	SiO_2	Al_2O_3	Fe_2O_3	TiO_2	CaO	MgO	K_2O	Na_2O	SO_3	LOI
Kaolinite	53.5	42	1.3	1.5	0.2	0.3	0.4	0.2	0	0.6
Illite	54	27	6	1	0.8	2.5	5.5	0.5	0.1	2.6
Montmorillonite	60	20	5	0.8	2	3.5	1.2	1	0.1	6.4
Limestone	1.5	0.6	0.2	0.05	54.5	0.8	0.1	0.1	0.2	41.95

A well-graded, clean siliceous sand conforming to EN 196-1 requirements [46,47] served as the aggregate phase. The sand possessed a maximum particle size of 2.0 mm and exhibited a continuous particle-size distribution (Figure 3), which supported improved packing density and stable layer-wise deposition during 3D printing [48,49].

Two chemical admixtures were incorporated to regulate fresh-state rheology for extrusion. A polycarboxylate-ether high-range superplasticiser (SP, ELMIERE SP 500) was used to maintain flowability at a low water-to-binder ratio. A viscosity-modifying agent (VMA) based on methylcellulose chemistry (CONMIX MgaAdd VE) was added to stabilise the mix under low-shear conditions, suppress bleeding, and ensure dimensional accuracy of the extruded filaments. These admixtures collectively facilitated the buildability and geometric fidelity required for the layer-by-layer printing process [35].

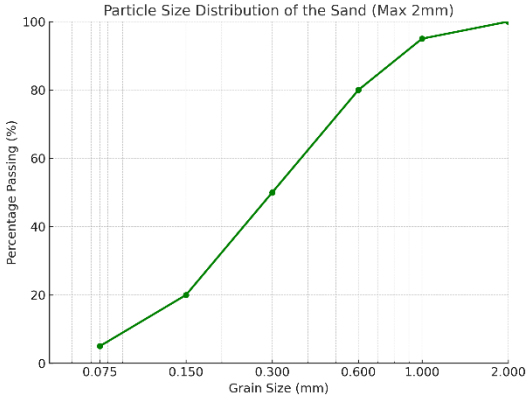

Figure 3. Particle size distribution of the fine siliceous sand used as the aggregate phase.

A physically activated (steam-activated) hardwood biochar, produced by Biochar Now, LLC (Colorado, USA), was used as the conductive carbonaceous phase. The material had a particle size ≤75 µm, bulk density of 0.35–0.45 g/cm³, and a Brunauer–Emmett–Teller (BET) surface area of approximately 700–1100 m²/g. Its morphology is shown in Figure 4a.

Natural GH fibres were incorporated as the reinforcement phase. The fibres were cut to a length of 8 ± 2 mm (6–10 mm range) and exhibited a tensile strength of approximately 130–160 MPa, elastic modulus of 2.5–3.5 GPa, and elongation at break of 20–30%, in line with reported values for keratin-based animal fibres. Their surface morphology is shown in Figure 4b.

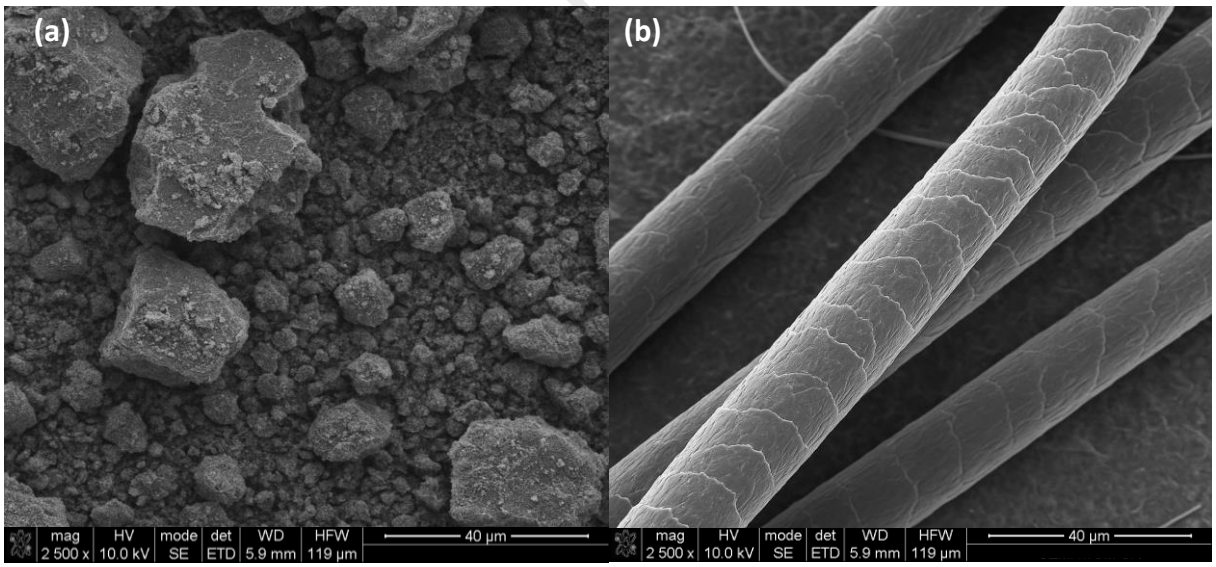

Figure 4. Scanning electron micrographs of the functional additives used in the LC³–biochar composites: (a) physical morphology of the powdered biochar, (b) surface topology of goat-hair fibres (GH), displaying the typical overlapping cuticle-scale pattern of animal keratin fibres.

2.2. Mixing and printing method

In this study, 40% of the OPC was replaced with an LC³ binder blend composed of 60% calcined kaolinite, 5% calcined illite, 5% calcined montmorillonite, and 30% limestone. All these LC³ proportions, together with the key mixture parameters—including the water-to-binder ratio (w/b) of 0.35, sand-to-binder ratio (s/b) of 1.5, and admixture dosages of 2.0 wt% SP and 1.5 wt% VMA—were previously optimised in our earlier research [2–5] through a combined experimental–machine-learning framework using a large multi-

variable materials database. These three clay minerals were selected because kaolinite, illite, and montmorillonite constitute the dominant clay fractions in most natural deposits worldwide—including those in Oman—and the optimisation aimed to enable direct utilisation of raw deposits without purification, thereby eliminating energy-intensive beneficiation steps [2–5]. Building on this optimised baseline formulation, the present study incorporates BC at a fixed dosage of 4.25 wt% of binder, selected from the electrical percolation threshold identified experimentally; the corresponding percolation curve is shown in Figure 5. GH fibres were introduced at volumetric fractions of 0, 0.4, 0.8, 1.2 and 1.6 vol%, with a target fibre length of 8 ± 2 mm, consistent with values reported in the literature for natural animal-hair reinforcements in cementitious composites [21,50]. The fibres were washed with distilled water and air-dried prior to mixing to remove oils and surface impurities that could hinder fibre–matrix bonding; no chemical pretreatment was used; as previous studies have shown that GH fibres disperse effectively without alkaline activation. Sample identifiers follow the notation BC4.25–GH–x, where x corresponds to the fibre volume fraction. For reference, BC4.25–GH–0 and the BC0–GH–0 (OPC+LC³ without BC or GH) mixes serve as the baseline materials used for comparison throughout this study.

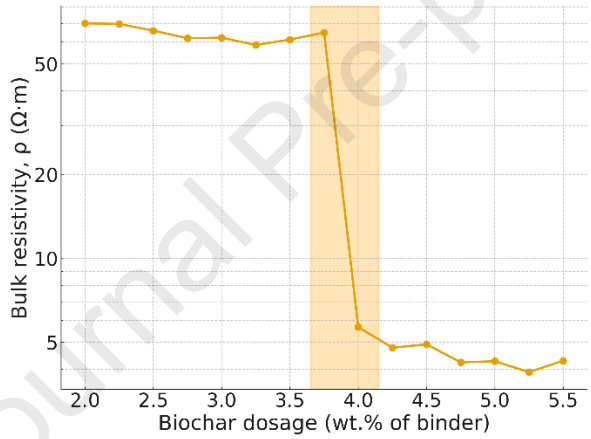

Figure 5. Bulk electrical resistivity (ρ) of the LC³–biochar composite as a function of biochar dosage (wt.% of binder). A pronounced percolation transition is observed between 3.8–4.2 wt.%, highlighted by the shaded region.

All materials were blended in a planetary mixer using a controlled multi-stage mixing sequence to ensure homogeneous particle dispersion and stable early-age structuration, and the overall mixing procedure is illustrated in Figure 6. Immediately after mixing, the fresh mortar was transferred to the extrusion system to prevent thixotropic rebuilding. Printing was performed using a 3D Potterbot Scara V4 robotic platform (Figure 7) with a 15 mm circular nozzle at 20 ± 2 °C and 55% relative humidity, employing a constant deposition speed of 20 mm/s and a 30-second interval between successive layers. The nozzle height was raised by 8.5 mm for each layer to match the actual filament thickness. This printing protocol follows the same procedure previously established and validated in our earlier LC³-based 3D printing studies. After printing, the specimens were kept under laboratory ambient conditions for approximately 24 h to ensure initial setting and shape stability. Subsequently, they were transferred to a curing room and cured at 20 ± 2 °C and relative humidity higher than 95% until the designated testing ages.

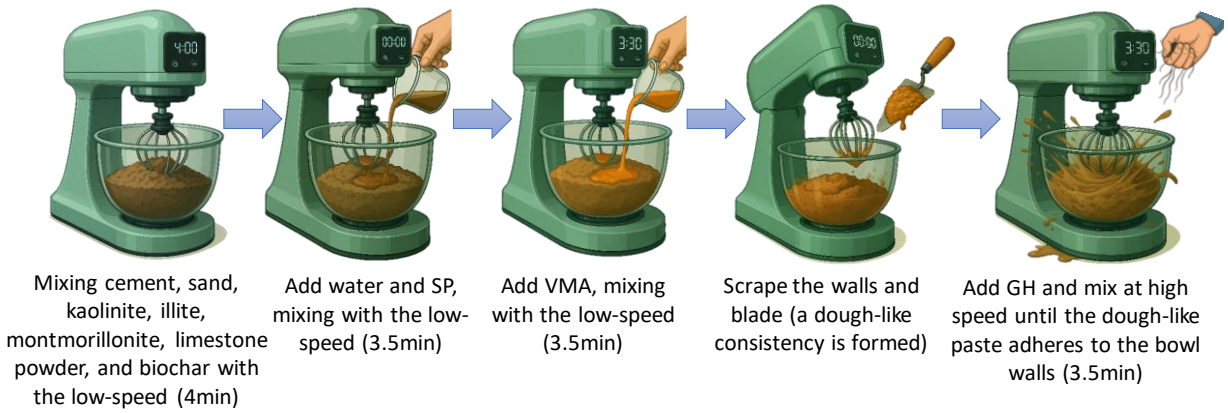

Figure 6. A schematic illustration of the mixing protocol adopted for preparing the LC³ composites.

Figure 7. 3D printing setup used for fabricating LC³–biochar–GH specimens in this study.

2.3. Rheology assessment

The rheological properties of the fresh LC³–biochar–GH mixtures were characterised using an ICAR Plus rheometer (Germann Instruments, Denmark) equipped with a cylindrical vane (radius 63.5 mm, height 127 mm) rotating inside a 143 mm container. This geometry ensured a stable shear field and prevented wall-slip effects, which is essential for mixtures containing carbonaceous particles and short natural fibres. All measurements were performed at 20 ± 2 °C. A controlled descending shear-rate protocol was applied by reducing the rotation speed from 0.50 to 0.05 rps in seven steps, each held for 5 s to allow torque stabilisation. The resulting shear-stress data were fitted to both the Bingham and Herschel–Bulkley constitutive models. The Bingham model was used to estimate extrusion-relevant yield stress and plastic viscosity, while the Herschel–Bulkley model captured the shear-thinning response introduced by biochar and goat-hair fibres, which cannot be represented by a linear model alone. To ensure comparability across all mixes, rheological measurements were taken immediately after mixing—without resting time—to avoid structural rebuilding effects [51]. The extracted yield stress and plastic viscosity values were subsequently used to interpret the influence of LC³ replacement, biochar percolation behaviour, and GH fibre volume fraction on extrusion stability and early structural build-up.

2.4. Mechanical performances assessment

The mechanical response of the 3D-printed LC^3–biochar–GH composites was quantified through compressive and flexural testing at curing ages of 3, 7, and 28 days, enabling evaluation of early-age development and long-term strength. Compressive loading was applied in two orthogonal orientations (Figure 8a). In the first configuration, the force was imposed perpendicular to the build direction, focusing on the integrity of the interlayer interfaces. The second configuration involved loading parallel to the filament deposition path, capturing the intrinsic material resistance along the continuous printed filaments. Tests were carried out on a universal testing machine under displacement control at 2 mm/min, following ASTM C109/C109M [4], in an environment maintained at 20 ± 2 °C and 55 ± 5% RH. Flexural performance was assessed via three-point bending tests (Figure 8b), again considering the same two orientations to capture anisotropic behaviour. For both directions, specimens were placed on cylindrical steel rollers with a 100 mm span, and bending was applied at 1 mm/min in accordance with ASTM C78/C78M [5][52]. The contrasting behaviours under loading normal and parallel to the layers provided insight into the coupling between filament morphology, and interlayer bonding, induced by LC^3 replacement, biochar percolation, and GH fibre addition.

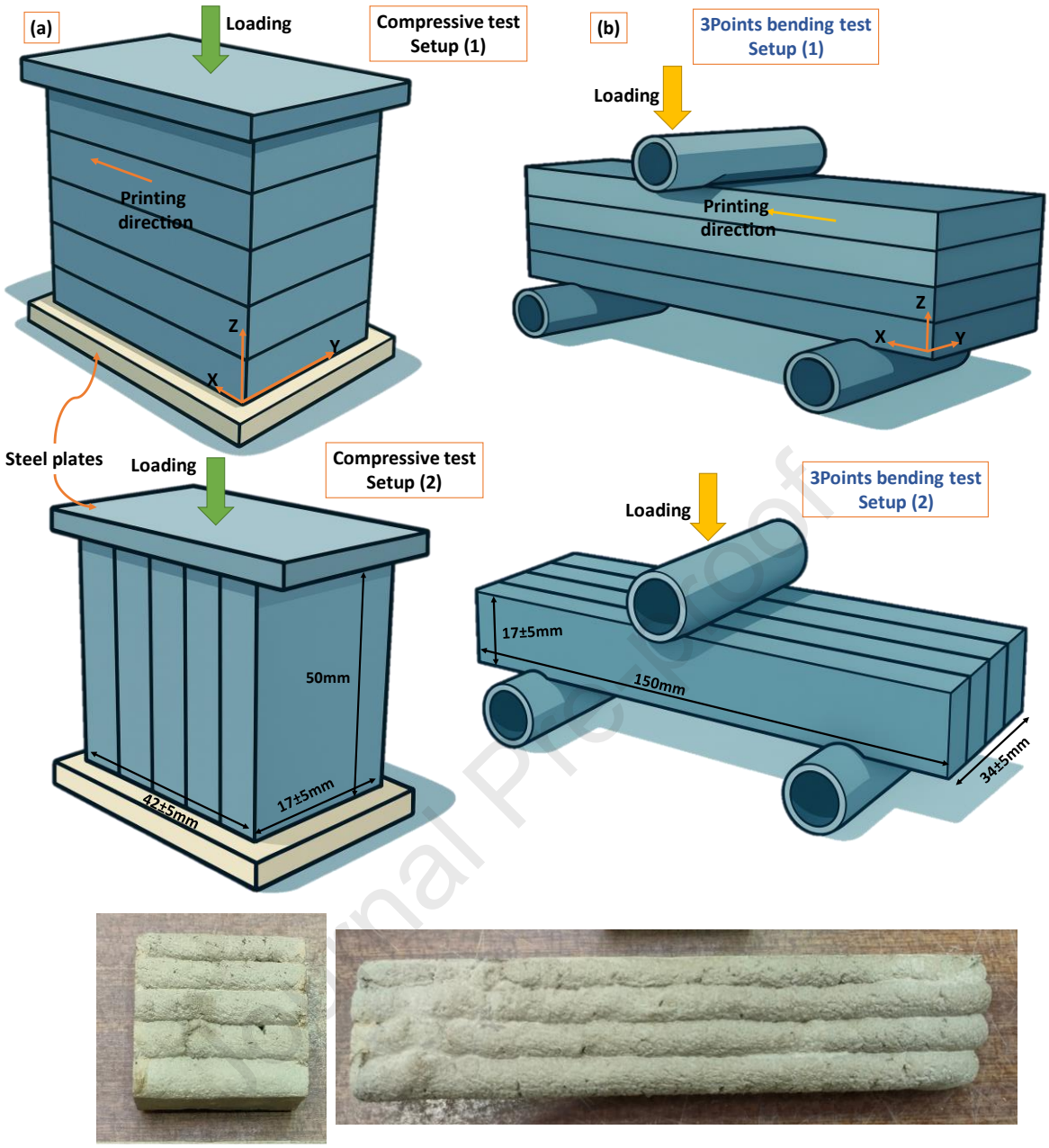

Figure 8. A schematic of mechanical testing configurations: (a) compressive test, (b) flexural test.

2.5. Effect of elevated temperatures on compressive strength

The details of this section have been presented in Appendix A.

2.6. Effect of combined acid–chloride exposure on compressive strength

The details of this section have been presented in Appendix A

2.7. Self-Sensing Behaviour under Cyclic Loading

2.7.1. Experimental Cyclic Piezoresistive Response

The self-sensing response of the printed cementitious composites was investigated under cyclic compressive loading using the electromechanical setup illustrated in Figure 9. Copper electrodes with dimensions of 50 mm × 10 mm × 0.3 mm were embedded during the printing process between the second and third printed layers to ensure stable internal electrical contact. The electrodes were connected to a high-precision digital multimeter through a two-probe configuration for continuous resistance monitoring during

loading with a rate of 60 Hz (synchronized with the mechanical measurements). It is noted that although the two-probe configuration may be influenced by contact resistance, this effect was minimized in the present study by embedding the copper electrodes outside the primary loading zone and by employing a perforated (mesh-like) electrode geometry to enhance interfacial contact and electrical continuity.

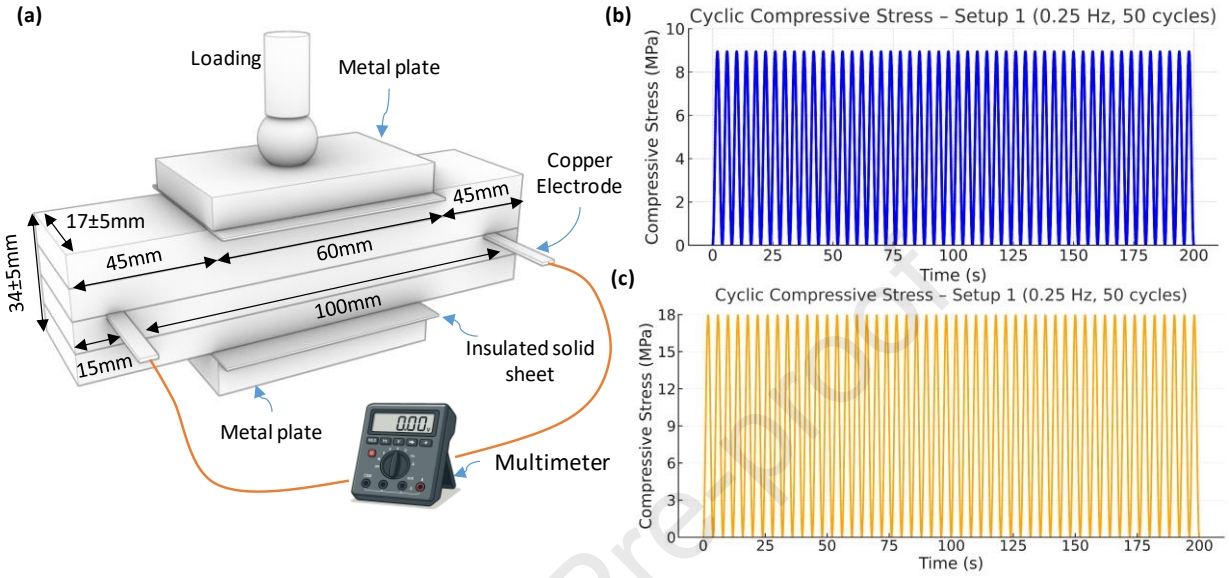

Figure 9. (a) Experimental setup for cyclic piezoresistive compression testing, (b) Loading protocol at 30% of the compressive strength (≈9 MPa), (c) Loading protocol at 60% of the compressive strength (≈18 MPa).

50 consecutive cycles (0.25 Hz) of compressive loading was applied under force control as shown in Figure 9 b and c. Two stress amplitudes were selected, corresponding to approximately 30% (≈9 MPa) and 60% (≈18 MPa) of the monotonic compressive strength. These two loading levels were intentionally chosen to activate two distinct electromechanical regimes, namely a predominantly elastic microcracking regime and a stable damage accumulation regime. During the tests, compressive stress, axial strain, and electrical resistance were recorded synchronously. The electrical signal was expressed as the fractional change in resistance (FCR), defined as the normalized resistance variation with respect to the initial unloaded state.

2.7.2. Machine-Learning Framework for Multi-Output Self-Sensing Prediction

A unified multi-output machine-learning framework was developed to capture the strongly coupled mechanical–electrical–damage response of the self-sensing cementitious composites under cyclic loading. The integrated dataset was constructed by combining the cyclic measurements obtained under both 30% and 60% stress amplitudes for all tested specimens. The dataset was derived from five independent specimens produced in five separate batches for each mix design, thereby capturing inherent variability arising from material processing, mixing, and 3D printing conditions. Each specimen was subjected to cyclic compressive loading consisting of 50 cycles at two stress levels. The prediction task was formulated as a simultaneous multi-target problem involving four physically coupled outputs, namely compressive stress, axial strain, instantaneous elastic modulus, and a scalar damage index using the instantaneous absolute fractional change in resistance (|FCR|).

The input feature vector was explicitly defined to represent the instantaneous electromechanical state of the material, consisting of (i) the absolute fractional change in resistance (|FCR|), and (ii) one-hot encoded specimen identifiers to account for inter-specimen variability. No derivative (e.g., d|FCR|/dt), lagged, cyclic index, or time-dependent features were included, in order to preserve a direct instantaneous mapping between the sensing signal and the predicted outputs. This design choice ensures physical interpretability and prevents the introduction of implicit temporal or history-dependent information into the model inputs.

The instantaneous elastic modulus was extracted directly from the synchronized stress–strain response at each loading increment using time-resolved secant stiffness evaluation, allowing tracking of progressive stiffness degradation within each cycle and across the entire loading history. The damage index was formulated as a hybrid physics-informed scalar parameter that simultaneously accounts for stiffness degradation, irreversible FCR drift, enlargement of electromechanical hysteresis loops, and cumulative deterioration induced by repeated cyclic loading. The damage index was mathematically defined as a normalized cumulative degradation parameter expressed as Eq.1:

$$D = 1 - \left({}^{E_{inst}}/_{E_0}\right) \quad \text{(Eq.1)}$$

where E_{inst} is the instantaneous secant modulus extracted at each loading increment, and E_0 is the initial elastic modulus measured at the undamaged state. This formulation ensures that the damage index remains physically bounded between 0 (undamaged state) and 1 (fully degraded state), while maintaining direct mechanical interpretability. The use of stiffness-based damage is physically justified by the strong sensitivity of elastic modulus to microcrack initiation, crack coalescence, and progressive structural degradation under cyclic compression.

Two nonlinear ensemble-based regression architectures were implemented within this unified multi-output framework, namely Random Forest and Extreme Gradient Boosting (XGBoost). In both cases, a single model was trained to predict all four output targets simultaneously, enabling the explicit learning of cross-correlations between mechanical, electrical, and damage-related variables. The Random Forest architecture was constructed as an ensemble of independently trained decision trees using bootstrap aggregation, where each tree recursively partitions the feature space based on optimally selected split points to minimize the prediction error [5]. The ensemble averaging mechanism provides strong robustness against noise, nonlinear coupling, and multicollinearity among input variables. The Random Forest model was implemented using 200 decision trees with no restriction on maximum depth, allowing full representation of nonlinear interactions within the dataset.

In parallel, the XGBoost architecture was formulated as a gradient-boosted ensemble of shallow regression trees trained sequentially, where each new learner corrects the residuals of the preceding ensemble. Regularization, learning-rate control, and subsampling strategies were employed to enhance generalization and numerical stability under the highly nonlinear electromechanical response.

The XGBoost model was configured with 400 boosting iterations, a maximum tree depth of 4, and a learning rate of 0.05. Subsampling ratios of 0.8 were applied to both rows and features to improve generalization and mitigate overfitting. The models hyperparameters were determined through empirical optimization combined with cross-validation to ensure stable and generalizable performance.

The selection of Random Forest and XGBoost was motivated by their complementary learning mechanisms and their proven robustness for strongly nonlinear, noisy, and multi-physics datasets [5]. Random Forest provides high stability and variance reduction through ensemble averaging of decorrelated trees, making it highly resistant to measurement noise and local overfitting [4]. In contrast, XGBoost is a powerful gradient-boosted architecture capable of capturing subtle nonlinear dependencies and higher-order feature interactions through sequential residual learning [3]. The simultaneous use of these two conceptually distinct ensemble paradigms enables a rigorous comparison between bagging-based and boosting-based multi-output learning strategies for cyclic self-sensing prediction [5].

To ensure a physically consistent evaluation and to prevent data leakage between training and testing sets, a group-based data partitioning strategy was adopted, in which the dataset was split according to specimen identity. All data points from a given specimen were exclusively assigned to either the training or testing subset, ensuring that the models were evaluated on entirely unseen material realizations.

Model performance and stability were assessed using the coefficient of determination (R^2), root mean square error (RMSE), and five-fold group-based cross-validation, in which all data points belonging to each specimen were kept within the same fold. At each iteration, four subsets were used for model training and the remaining subset was used for independent validation, ensuring that each data point was tested exactly once. This procedure provides a statistically robust estimation of model generalization capability and prevents bias induced by a single train–test split. In addition, feature importance analysis was performed (reported in the Results section) to quantify the relative contribution of each input variable and to enhance the interpretability of the proposed multi-output learning framework. This minimal feature representation enables the development of a sensing-driven predictive framework, in which the mechanical state is inferred directly from the electrical response without requiring explicit knowledge of loading conditions.

For full transparency, reproducibility, and further verification, the complete machine-learning scripts used for Random Forest and XGBoost multi-output training are provided in the Appendix B

2.8. CO_2 Uptake Measurement

CO_2 uptake of the LC^3–biochar composites was measured using a laboratory-scale stainless-steel flow micro-chamber system operated under continuous CO_2 exposure with a volume of 130 ± 5 mL. The chamber was equipped with a calibrated pressure gauge (0–2.5 MPa), one CO_2 inlet fitted with a fine needle valve for flow control, and one outlet connected directly to a CO_2 concentration measurement line under strictly controlled conditions.

Each specimen was prepared in a coin-shaped geometry with a diameter of 30 ± 0.5 mm and a thickness of 5.0 ± 0.2 mm. During the test, the specimen was placed directly on a conductive copper coil substrate

and connected externally for real-time resistance monitoring during CO_2 exposure. The experimental CO_2 chamber, sensing coil, and specimen used for the uptake test are illustrated in Figure 10.

Pure CO_2 gas with a purity of 99.99% was supplied at a constant volumetric flow rate of 100 mL/min using a flowmeter. All tests were carried out at 24–25 °C under ambient laboratory relative humidity (≈ 50–55% RH). Each adsorption test was conducted continuously for 30 days.

The outlet CO_2 concentration, $C_{out}(t)$, was continuously recorded using a non-dispersive infrared (NDIR) CO_2 sensor, which was calibrated prior to testing. The inlet concentration C_{in} remained constant at 100% throughout all experiments. The breakthrough behavior observed in the outlet signal was used to quantify the adsorption dynamics. The cumulative CO_2 uptake per unit exposed area, q(t) (g/m²), was calculated from the inlet–outlet concentration difference using Eq.2:

$$q(t) = (1/A) \int_0^t Q[C_{in} - C_{out}(t)]dt \quad \text{(Eq.2)}$$

where Q is the gas flow rate (m³/s), A is the exposed specimen area (7.07×10^{-4} m²), and C_{in}, C_{out} are CO_2 concentrations converted to mass units. The integration was performed numerically using the discrete form:

$$q(t_i) = q(t_{i-1}) + \left(\frac{Q}{A}\right)[C_{in} - C_{out}(t_i)]\Delta t \quad \text{(Eq.3)}$$

where $q(t_i)$ is the CO_2 uptake at time t_i, $q(t_{i-1})$ is the uptake at the previous time step, Q is the CO_2 flow rate, A is the exposed surface area of the specimen, C_{in} and C_{out} are the inlet and outlet CO_2 concentrations, and Δt is the time interval between measurements.

After completion of each 30-day adsorption cycle, specimens were regenerated by heating at 60 °C for 48 h, followed by cooling to room temperature. No chemical washing was applied. This regeneration procedure was repeated in successive cycles to evaluate the cyclic adsorption capacity and long-term operational stability of the system.

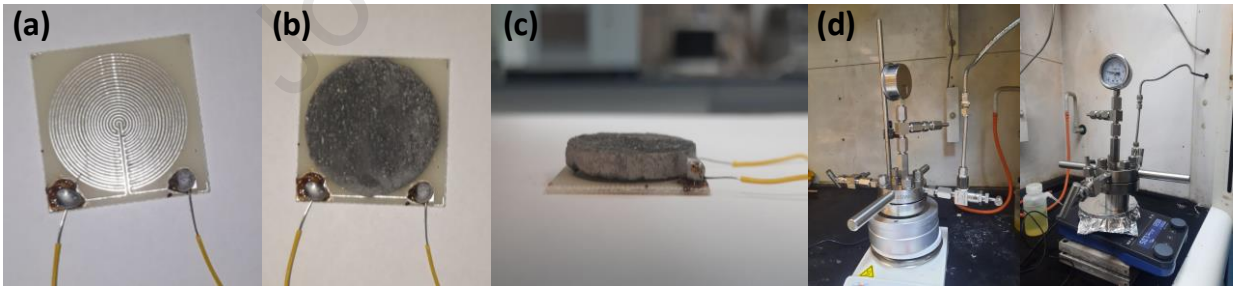

Figure 10. The experimental CO_2 measurement setup: a) sensing coil, b) and c) specimen, d) micro-chamber used for the uptake test.

2.9. Microstructural analysis

High-resolution SEM imaging was carried out using a FEI NOVA NanoSEM 200 equipped with a field-emission gun. Samples were obtained from the mid-height region of printed elements and prepared as small fragments of approximately 10 × 10 × 10 mm. The specimens were gently fractured to expose natural failure surfaces and sputter-coated with a 30 nm Au–Pd conductive layer (Cressington 208HR). Imaging was performed under secondary-electron (SE) mode at 10 kV accelerating voltage, enabling

clear visualization of the LC³ gel morphology, biochar particle interfaces, fibre–matrix transition zones, and microcrack features induced by printing or loading.

Thermal decomposition behavior was assessed through TGA/DTG using a PerkinElmer STA system. Samples were collected, weighed per group, ground and crushed, and then sieved through a 200-mesh screen to ensure uniform particle size. Finely ground specimens (≈20 mg) were heated from room temperature to 1000 °C at a constant rate of 10 °C/min under nitrogen (N_2) flow (100 mL/min) to prevent oxidation [53]. Mass-loss intervals corresponding to free/bound water release, portlandite dehydroxylation, carbonate decomposition, and secondary phase breakdown were identified to evaluate the extent of LC³ hydration, carbonation, and biochar–binder interactions.

Pore structure was further quantified using Mercury Intrusion Porosimetry (MIP). Samples were crushed into fragments of approximately 5 mm and immersed in ethanol for 7 days prior to testing to prevent further hydration reactions. Each sample had a mass of approximately 3 g. Intrusion–extrusion curves were obtained using a high-pressure porosimeter capable of pressures up to 227 MPa, with a mercury contact angle of 140°, allowing intrusion into pores down to ~5 nm [54]. The results of this section has been presented in Appendix A.

3. Results and discussion

3.1. Rheology assessment

3.1.1. Flow curve analysis

Figure 11 shows the steady-shear response of the LC³–biochar–GH mortars in terms of shear stress (τ) and apparent viscosity (η) as a function of shear rate ($\dot{\gamma}$). The shear stress–shear rate curves exhibit a pronounced non-linear increase over the investigated range (≈4–30 s^{-1}), with τ rising from about 780–1000 Pa at $\dot{\gamma} \approx 4$ s^{-1} to 1180–1330 Pa at $\dot{\gamma} \approx 30$ s^{-1}. The reference LC³ mixture without biochar or fibres (BC0-GH-0) consistently develops the lowest stresses, whereas the addition of 4.25 wt.% biochar (BC4.25-GH-0) shifts the entire curve upward by roughly 80–120 Pa across the shear-rate window. Further incorporation of GH produces an additional increase in τ, particularly at low and intermediate $\dot{\gamma}$, with BC4.25-GH-1.2 and BC4.25-GH-1.6 reaching stresses close to 1300 Pa at the highest shear rates. Despite these differences in absolute level, all mixtures show similar curvature and gradually converging trends at $\dot{\gamma} > 20$ s^{-1}, indicating comparable resistance in the high-shear extrusion regime.

The corresponding apparent viscosity curves confirm a strong shear-thinning behaviour typical of flocculated cementitious suspensions. At $\dot{\gamma} \approx 4$ s^{-1}, η lies in the range of 300–330 Pa·s for all compositions; as the shear rate increases to ≈30 s^{-1}, η rapidly decays to ≈40–45 Pa·s, with only minor differences between mixes. The reference BC0-GH-0 mixture again exhibits the lowest viscosity envelope, while the introduction of biochar and GH initially increases η at very low $\dot{\gamma}$ but does not penalise the high-shear regime relevant for pumping and extrusion. This rheological window, combining relatively high resistance at rest/low shear with marked viscosity reduction under flow, falls within the range reported as suitable for 3D-printed mortars and ultra-high-performance printable concretes, where static yield stress is typically of

the order 500–1500 Pa and strong shear thinning is considered essential for buildability and extrudability [55–59].

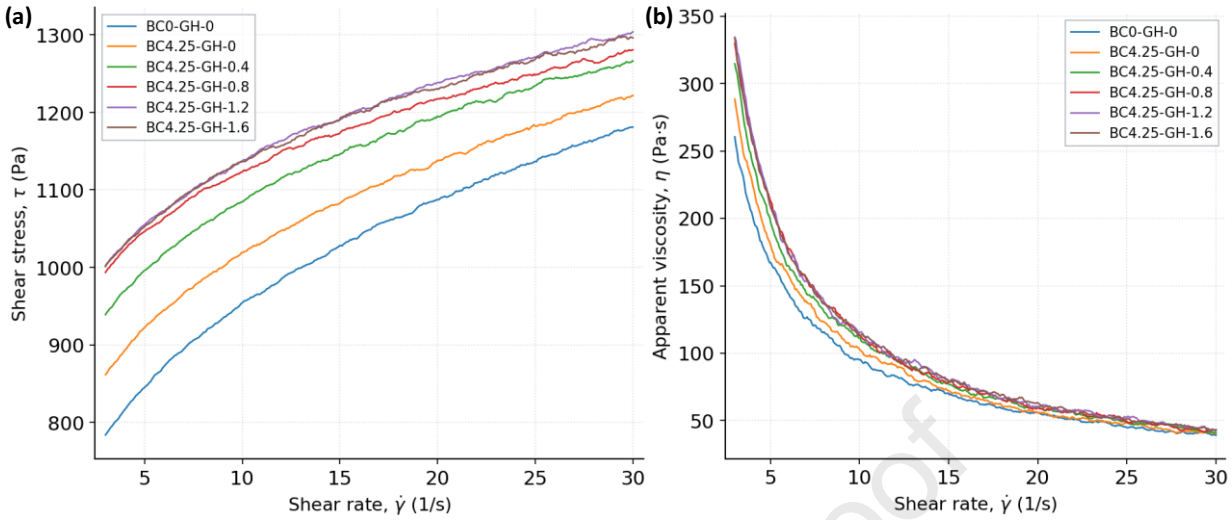

Figure 11. Flow curve analysis of the cementitious composites. (a) Shear stress–shear rate flow curves of LC³–biochar–GH mixtures, showing increased stress levels with biochar addition and further enhancement with rising GH content; (b) Apparent viscosity profiles demonstrating strong shear thinning for all mixes, with convergence at high shear rates. The combined response defines a rheological window suitable for extrusion-based 3D printing. (SD ≤ 7%).

To quantify these observations and enable comparison with rheological criteria proposed for 3DCP, the descending-rate branches of the flow curves were fitted using both the Bingham and Herschel–Bulkley models. These constitutive laws are widely adopted for cementitious systems because they capture a finite yield stress and a shear-rate-dependent viscosity with only two or three parameters, and their parameters can be directly related to pumpability, extrudability and structural build-up [55,57,58,60]. The fitted parameters for all mixtures are summarised in Table 3 and Table 4. The Bingham model provides an operational yield stress and plastic viscosity that are convenient for engineering design, whereas the Herschel–Bulkley model allows a more accurate description of the shear-thinning exponent [61]. Taken together, these two fits delineate an effective yield-stress window and viscosity envelope for the LC³–biochar–GH samples.

Table 3. Herschel–Bulkley fitting parameters for the LC³–biochar–GH mixtures, including yield stress (τ_0), consistency index (k), flow index (n), and coefficient of determination (R^2). The results show a progressive increase in τ_0 with biochar incorporation and rising GH content, while n < 0.5 across all samples confirms pronounced shear-thinning behaviour.

Sample	τ_0 (Pa)	k (Pa·s^n)	n	R^2 (Herschel–Bulkley)
BC0-GH-0	452.37	170.69	0.457	0.860
BC4.25-GH-0	563.92	314.67	0.194	0.830
BC4.25-GH-0.4	591.48	326.84	0.194	0.900
BC4.25-GH-0.8	638.71	352.04	0.171	0.840
BC4.25-GH-1.2	689.33	191.69	0.335	0.880
BC4.25-GH-1.6	741.26	282.59	0.176	0.810

Table 4. Bingham fitting parameters for the LC³–biochar–GH mixtures, including yield stress (τ_0), plastic viscosity (μ_p), and coefficient of determination (R^2). The data show a clear increase in τ_0 with the incorporation of biochar and moderate GH

dosages, while μ_p decreases substantially relative to the Plain matrix, indicating improved flowability at extrusion-relevant shear rates.

Sample	τ_0 (Pa)	μ_p (Pa·s)	R^2 (Bingham)
BC0-GH-0	741.92	17.856	0.87
BC4.25-GH-0	969.62	7.615	0.82
BC4.25-GH-0.4	926.62	13.781	0.89
BC4.25-GH-0.8	1056.85	6.438	0.84
BC4.25-GH-1.2	1094.82	6.162	0.81
BC4.25-GH-1.6	974.16	12.605	0.88

It is important to note that the Bingham model is known to systematically overestimate the true yield stress of cementitious suspensions, particularly in mixtures exhibiting strong shear thinning [61]. This behaviour arises because the linear τ–$\dot{\gamma}$ form forces the fitted line to intersect the low-shear curvature of the experimental data, artificially elevating τ_0 to compensate for non-linearity [62,63]. In contrast, the Herschel–Bulkley model, through its non-linear exponent $n < 1$, provides a more faithful representation of the low-shear regime and therefore yields τ_0 values that are generally closer to the intrinsic static yield stress reported for cementitious and LC³-based systems [61]. Consequently, the HB-derived τ_0 values in this study should be interpreted as the more physically representative estimates, while the Bingham parameters remain operational indicators useful for engineering comparison and pumpability assessment [55,57,58,60]. Accordingly, the Herschel–Bulkley yield stress was adopted as the primary parameter for subsequent analysis, interpretation, and optimisation.

The Herschel–Bulkley fits indicate that the apparent yield stress τ_0 increases almost monotonically from 452 Pa for BC0-GH-0 to 564 Pa for BC4.25-GH-0 and to 591, 639, 689 and 741 Pa for GH contents of 0.4, 0.8, 1.2 and 1.6 vol%, respectively. The consistency index k remains within 170–352 Pa·s^n, while the flow index n is consistently below 0.5, confirming strong shear-thinning behaviour across all mixtures. The Bingham representation yields higher τ_0 values—742 Pa for BC0-GH-0 and 970–1095 Pa for the biochar- and fibre-reinforced mixes—but follows the same global trend, with a moderate plateau between 0.4 and 1.2 vol% GH and a slight drop at 1.6 vol%. In parallel, the plastic viscosity μ_p decreases from 17.9 Pa·s in the reference mixture to 7.6 Pa·s when 4.25 wt.% biochar is added, reaching minima of 6.4–6.2 Pa·s at 0.8–1.2 vol% GH before increasing again to 12.6 Pa·s at 1.6 vol%. These values imply that the LC³–biochar system shifts the mortar towards a rheological domain characterised by elevated yield stress but reduced plastic viscosity—a combination often highlighted as desirable for printable concretes because it promotes shape stability without excessively increasing pumping pressure [56–59,64].

The fitted yield stresses can be contextualised against published thresholds for buildable 3DCP mixtures. Several studies suggest that printable concretes require static yield stresses on the order of 500–1000 Pa (or even up to ≈1500 Pa for very stiff systems) to prevent layer collapse and excessive deformation under self-weight and subsequent layers [56–59,65]. In this study, the reference LC³ mortar BC0-GH-0 already

attains an effective yield stress of around 700 Pa when the Bingham and Herschel–Bulkley fits are interpreted together, which is consistent with the static yield stress obtained independently from the stress-growth tests discussed later in Section 3.1.2. The incorporation of biochar and GH shifts τ_0 further into the central part of the recommended printability window while maintaining moderate plastic viscosities. This evolution confirms that the rheology of the LC³-based system has been steered towards a regime that supports both pumpability and green strength [2].

The underlying mechanisms responsible for this rheological evolution can be interpreted in terms of the coupled effects of LC³ chemistry, biochar porosity, and fibre reinforcement. Replacing 40% of OPC with the LC³ blend (60% calcined kaolinite, 5% illite, 5% montmorillonite, 30% limestone) increases the specific surface area and solid volume fraction of the binder, promoting flocculation and a stronger interparticle network at rest [35,60,66,67]. Calcined kaolinite contributes highly reactive aluminosilicate phases that generate C–A–S–H gel and refine the microstructure, while the fine limestone acts as a nucleation site and filler, enhancing packing density [4,5]. Montmorillonite and illite, even at modest fractions, are known to increase water adsorption and static structuration, thereby elevating yield stress and thixotropic build-up [35,66,67]. These LC³-driven effects explain why the reference BC0-GH-0 mixture already sits near the lower bound of the printable yield-stress interval rather than behaving like a conventional OPC mortar.

Superimposed on this LC³ backbone, biochar addition exerts a dual influence on the fresh behaviour. Several recent studies have shown that cement pastes and mortars containing 2–10 wt.% biochar typically exhibit increased static yield stress and enhanced thixotropy, attributed to the high internal surface area, hierarchical porosity and irregular morphology of biochar particles [68–70]. The porous structure of biochar absorbs mixing water and promotes internal curing, while its rough surface fosters mechanical interlocking within the particle network [71]. As a result, the matrix becomes more cohesive at low shear, which explains the ≈25% rise in τ_0 when moving from BC0-GH-0 to BC4.25-GH-0. At the same time, partial water sequestration and efficient dispersion by the polycarboxylate-based superplasticiser prevent excessive viscosity growth; in fact, μ_p is reduced by more than 50% compared with the reference mixture. Similar combinations of increased yield stress and controlled viscosity have been reported for biochar-modified eco-cements and have been associated with improved dimensional stability and reduced bleeding [68–70].

The progressive addition of GH further modifies the particle–fibre network. Low to moderate fibre contents are known to increase yield stress through mechanical interlocking and the formation of a load-bearing skeleton, while their impact on plastic viscosity depends on fibre length, aspect ratio and orientation under shear [56,58]. In the present series, increasing GH dosage from 0 to 1.2 vol% raises the Herschel–Bulkley τ_0 by about 22% (from 564 to 689 Pa) without a systematic penalty in μ_p, which reaches its minimum near 0.8–1.2 vol%. This suggests that the goat hair fibres effectively reinforce the flocculated LC³–biochar skeleton at rest, but tend to align with the flow direction under shear, limiting additional viscous dissipation. At 1.6 vol% GH, the slight increase in μ_p and the marginal reduction in Bingham τ_0 indicate the onset of

fibre congestion and local heterogeneities, which is consistent with the expected transition from a well-dispersed to a partially entangled fibre network at higher volume fractions [56,58].

From a 3D-printing perspective, these results highlight BC4.25-GH-0.8 as a particularly favourable compromise: this mixture combines an effective yield stress in the middle of the recommended buildability window with one of the lowest plastic viscosities in the series [57]. Such a rheological envelope is expected to support robust filament shape retention and interlayer stability, while maintaining acceptable pumping pressures and nozzle flow during printing [57,58]. This interpretation is consistent with recent rheology–printability frameworks that identify a narrow band of yield stress–viscosity combinations as optimal for defect-free extrusion of cementitious materials [57–59,64,65]. The subsequent stress-growth analysis (Section 3.1.2) further substantiates this conclusion by demonstrating that the same compositions also exhibit favourable time-dependent structuration and static yield-stress evolution.

3.1.2. Stress growth test

Figure 12 shows the variation of shear stress and torque with time during the stress-growth tests for the LC³–biochar–GH mixtures. After the vane starts rotating at the constant speed (0.025 rps), all mixtures exhibit a rapid stress build-up over the first ≈3–4 s, followed by a distinct overshoot and a subsequent gradual decay towards a quasi-steady state. The reference LC³ mortar without biochar or fibres (BC0-GH-0) reaches the lowest peak shear stress, about 720 Pa, and then displays a continuous softening down to values close to 450–500 Pa at t = 60 s. When 4.25 wt.% biochar is introduced (BC4.25-GH-0), the peak increases to ≈880 Pa and the subsequent decay becomes less pronounced, indicating a more cohesive internal structure under shear. Further incorporation of GH increases the peak stresses to ≈940 Pa (BC4.25-GH-0.4) and ≈1000 Pa (BC4.25-GH-0.8), while BC4.25-GH-1.2 and BC4.25-GH-1.6 still reach relatively high maxima of ≈980 and ≈950 Pa, respectively. For all fibre-reinforced mixtures, the stress level remains significantly above that of BC0-GH-0 throughout the test, and the long-term decay is slower, highlighting enhanced structural robustness under sustained shearing. The torque curves in Figure 12b mirror these trends, confirming that the observed behaviour is intrinsic to the material response and not an artefact of the conversion to shear stress.

As can be observed, the shape of the stress–time curves is characteristic of thixotropic yield-stress fluids: an initial build-up of internal structure at rest, followed by a rapid mobilisation of this structure upon shearing, a maximum corresponding to the static yield stress, and a progressive breakdown towards a dynamic equilibrium state [55,57,72]. In this framework, the overshoot peak can be interpreted as an estimate of the static yield stress, whereas the long-term plateau represents the dynamic yield stress under the imposed shear rate [55]. As discussed before, rheological models such as Bingham and Herschel–Bulkley tend to capture primarily the dynamic branch of the response, and Bingham-derived τ_0 often overestimates the true yield stress, while Herschel–Bulkley parameters are generally closer to the intrinsic static value [62]. The present stress-growth results are consistent with this interpretation: for all mixtures, the overshoot peaks (720–1000 Pa for the most relevant compositions) lie slightly above the τ_0 values

obtained from Herschel–Bulkley fitting, while remaining within the buildability window (≈500–1500 Pa) typically reported for 3D printable concretes [57].

The comparison between mixes highlights the combined role of LC³, biochar and GH in controlling time-dependent structuration. The lowest peak and strongest decay observed for BC0-GH-0 indicate that, although the LC³ binder already provides a certain degree of flocculation and static structuring, the network formed at rest is relatively fragile and susceptible to shear-induced breakdown [2,4,5]. This is consistent with previous studies showing that LC³ systems, while more thixotropic than plain OPC pastes, still exhibit marked sensitivity to continuous shearing unless additional fines or structuring agents are present [60]. The increase in peak stress from 720 Pa to 880 Pa upon adding 4.25 wt.% biochar reflects the formation of a denser and more cohesive particle network. Biochar particles, with their high internal surface area and irregular morphology, enhance interparticle friction and mechanical interlocking, while their porous structure locally absorbs mixing water and promotes capillary-driven attraction, leading to a higher static yield stress and improved network stability under shear [35,69]. At the same time, the moderate decay of stress after the peak indicates that the biochar-stabilised structure does not collapse catastrophically but undergoes a controlled rearrangement towards a dynamic equilibrium [35].

The further increase in peak stress with GH addition, up to ≈1000 Pa for BC4.25-GH-0.8, can be attributed to the development of a fibre-supported skeleton superimposed on the LC³–biochar flocculated matrix. At low to moderate fibre volumes, long, flexible fibres are known to bridge neighbouring flocs and enhance load transfer, thereby increasing the static yield stress and resistance to structural collapse [55,73]. The slower stress decay and the relatively high stress level maintained over the entire 60 s window for BC4.25-GH-0.4 and BC4.25-GH-0.8 suggest that the fibre network effectively resists progressive breakdown and promotes partial restructuring under shear, which is beneficial for maintaining shape stability between successive printed layers [2]. The oscillations visible in the stress and torque signals of the fibre-reinforced mixtures, particularly at intermediate times, are consistent with intermittent fibre realignment and local stick–slip events within the particle–fibre skeleton, a behaviour frequently observed in fibre-rich cementitious suspensions [73–75].

At higher GH contents (1.2–1.6 vol%), the peak stress does not increase further and even slightly decreases from ≈1000 Pa to ≈950 Pa, while the stress decay becomes more pronounced and the signal more irregular. This trend can be interpreted as the onset of fibre congestion and heterogeneity: as the fibre volume increases, the probability of fibre clustering, local entanglement and poor dispersion rises, which can create weak zones and inhomogeneous stress transmission pathways [74,75]. These local defects may limit the effective contribution of fibres to the static yield stress and promote larger stress fluctuations under continuous shearing [2]. Thus, while 1.2–1.6 vol% GH still provides higher stress levels than the fibre-free mixtures, the rheological response becomes less stable and potentially more sensitive to processing conditions, which is undesirable for robust large-scale printing.

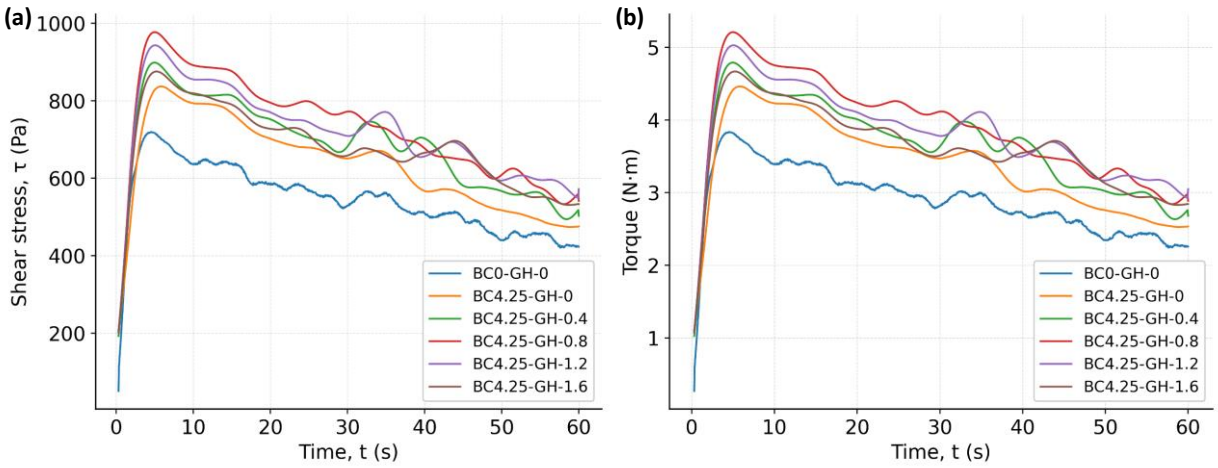

Figure 12. Stress growth analysis of the cementitious composites: (a) Stress-growth response of the LC³–biochar–GH mixtures under a constant shear rate (0.025 rps), showing rapid structuration, distinct overshoot peaks associated with static yield stress, and subsequent shear-induced breakdown. Peak stresses increase from ≈720 Pa (BC0-GH-0) to ≈880–1000 Pa with biochar and GH additions, reflecting enhanced flocculated network strength (SD ≤ 6%).

3.2. Mechanical Assessment

3.2.1. Compressive strength

Figure 13 presents the compressive strength behaviour of the LC³–biochar–GH mixtures tested under the two loading configurations. In Setup 1, where the load is applied perpendicular to the printing layers, the reference LC³ mixture without biochar or fibres (BC0-GH-0) reaches about 22, 30 and 34 MPa at 3, 7 and 28 days, respectively. Incorporating 4.25 wt.% biochar (BC4.25-GH-0) leads to a moderate reduction at all ages, with strengths of ≈19, 27 and 30 MPa (≈10–15% lower than BC0-GH-0 at 28 days). The addition of GH slightly compensates this loss at low to moderate dosages: BC4.25-GH-0.4 attains ≈20, 28 and 31–32 MPa, recovering part of the 28-day strength and approaching ≈95% of the reference LC³ value. For higher fibre contents, the strength decreases progressively; BC4.25-GH-0.8, BC4.25-GH-1.2 and BC4.25-GH-1.6 achieve ≈30, 27–28 and 24–25 MPa at 28 days, corresponding to reductions of roughly 10, 20 and 30% relative to BC0-GH-0. Higher fibre contents lead to increased voids and reduced load transfer, as supported by SEM observations of fibre–matrix debonding and MIP results indicating increased pore connectivity (Appendix A).

A similar trend is observed in Setup 2, where the load is applied parallel to the printing layers, but with systematically lower strength levels. The reference mixture develops ≈15, 21 and 24 MPa at 3, 7 and 28 days, while BC4.25-GH-0 reaches ≈12, 18 and 21 MPa (≈12–15% reduction at 28 days). As in Setup 1, a GH content of 0.4 vol% partially restores the strength, yielding ≈13, 19 and 22 MPa, whereas higher fibre volumes lead to a gradual decline: BC4.25-GH-0.8 and BC4.25-GH-1.2 reach ≈21 and 18–19 MPa at 28 days, and BC4.25-GH-1.6 falls to ≈16–17 MPa. Overall, Setup-1 strengths are about 30–40% higher than those of Setup 2 for a given mix, confirming a clear but not extreme mechanical anisotropy associated with the printing-induced layer orientation.

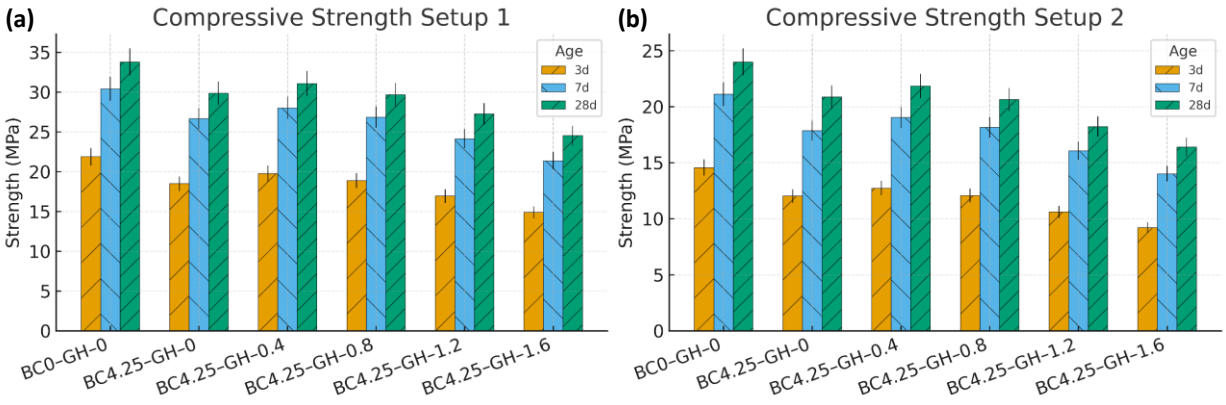

Figure 13. (a) Compressive strength of the LC³–biochar–GH mixtures under Setup 1 (loading ⊥ to printing layers) at 3, 7 and 28 days, showing the strength reduction induced by biochar and the partial recovery at low GH contents. (b) Corresponding results for Setup 2 (loading ∥ to printing layers), exhibiting lower strength levels and a similar ranking across mixtures, evidencing printing-induced anisotropy in the hardened response.

The corresponding 28-day elastic modulus values shown in Figure 14 follow the same ranking. In Setup 1, BC0-GH-0 exhibits an elastic modulus of ≈22 GPa, while the biochar-containing, fibre-free mix BC4.25-GH-0 decreases to ≈17 GPa. The mixture with 0.4 vol% GH displays a slight recovery to ≈18 GPa, but further increasing the fibre content reduces the modulus to ≈16, 13 and 11 GPa for 0.8, 1.2 and 1.6 vol% GH, respectively. Setup-2 moduli are consistently lower, around 18 GPa for BC0-GH-0 and decreasing to ≈13–14 GPa for BC4.25-GH-0 and BC4.25-GH-0.4, ≈13 GPa for BC4.25-GH-0.8, and ≈11 and 9–10 GPa for BC4.25-GH-1.2 and BC4.25-GH-1.6. These results indicate that both strength and stiffness penalties become significant at GH contents above 0.8 vol%, whereas the combination of 4.25 wt.% biochar with 0.4 vol% GH maintains compressive performance within a relatively narrow margin of the LC³ reference. The observed trends are consistent with the combined microstructural effects of LC³, biochar and natural fibres. The small but systematic reduction in compressive strength and modulus when replacing the LC³ reference matrix with the LC³–biochar system (BC4.25-GH-0) can be attributed to the increased total porosity and weaker stiffness of the porous carbonaceous inclusions, as commonly reported for biochar-modified mortars and concretes which is consistent with the pore-structure evolution observed in MIP analysis and SEM images (Appendix A). At the same time, as discussed before, biochar enhances structuration and yield stress in the fresh state, which promotes buildability and interlayer consolidation but does not necessarily translate into higher compressive capacity at 28 days. At low fibre volume (0.4 vol%), GH can bridge microcracks and locally redistribute stresses without introducing excessive defects, which explains the partial regain in strength relative to BC4.25-GH-0. For higher fibre volumes, however, the probability of fibre clustering, entrapped air and imperfect fibre–matrix interfaces increases, leading to stress concentrations and premature microcracking under compression and the interfacial features as shown in SEM images (Appendix A). This is reflected in the monotonic decrease in both strength and modulus for GH ≥0.8 vol% in both setups.

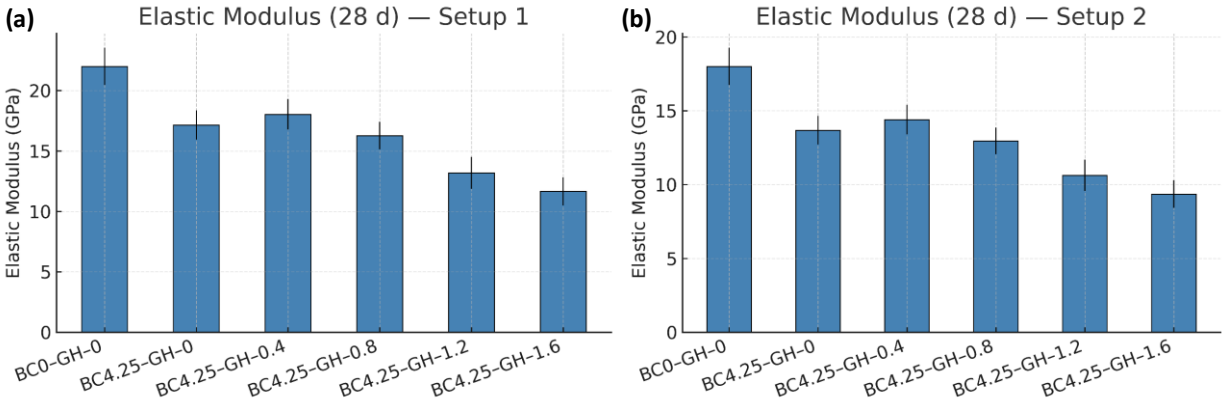

Figure 14. (a) Elastic modulus of the LC³–biochar–GH mixtures under Setup 1, indicating a progressive reduction in stiffness with increasing GH content and a moderate decline due to biochar addition. (b) Elastic modulus under Setup 2, reflecting the same decreasing trend and confirming lower stiffness parallel to the printing layers.

A comparison with existing literature highlights that the compressive strengths obtained in this study fall within the typical range reported for LC³-based mortars and biochar- or fibre-modified cementitious composites. For LC³ systems with 30–50% clinker replacement, 28-day strengths of 30–40 MPa are commonly reported, depending on clay reactivity and limestone fineness [6,60]. The 34 MPa value achieved by the LC³ reference (BC0-GH-0) in Setup 1 therefore aligns well with these benchmarks. When biochar is incorporated, strength reductions of 5–20% have been widely observed due to increased porosity and reduced matrix continuity [76]. The ≈10–15% decrease recorded for BC4.25-GH-0 in the present work is fully consistent with these trends. Regarding fibre reinforcement, several studies on cementitious composites have shown that low fibre volumes can maintain or slightly enhance compressive performance, whereas higher dosages often lead to significant reductions due to fibre clustering and poor compaction [77]. Considering that the goat hair fibres used here are relatively short (≈8 ± 2 mm) and of moderate aspect ratio, the modest loss of compressive strength at 0.4 vol% GH and the more pronounced decrease beyond 0.8 vol% are in strong agreement with literature: at low contents, fibres can bridge microcracks without severely disturbing packing, while at higher contents their random orientation and limited stiffness promote heterogeneities and stress concentrations [78]. Furthermore, the anisotropy ratio between Setup 1 and Setup 2 (≈1.3–1.4) matches the anisotropy levels reported for 3D-printed cementitious materials, where differences of 20–40% between perpendicular and parallel loading directions are typical due to filament alignment and interlayer morphology [79]. Overall, the mechanical response of the LC³–biochar–GH system is in strong agreement with the known behaviour of LC³ binders and fibre-reinforced cementitious composites, while enabling multifunctional capabilities not achievable with conventional OPC systems.

3.2.2. Flexural strength

Figure 15 summarises the flexural performance of the LC³–biochar–GH composites for both loading configurations. Across all curing ages, the reference LC³ mortar (BC0-GH-0) exhibits 28-day strengths of ≈3.9 MPa in Setup 1 and ≈3.0 MPa in Setup 2. The incorporation of 4.25 wt.% biochar (BC4.25-GH-0) yields comparable values, with 28-day strengths of ≈3.9 MPa (Setup 1) and ≈3.0 MPa (Setup 2), indicating that biochar alone does not compromise the tensile load-bearing capacity of the LC³ matrix. Introducing

GH fibres leads to a clear enhancement at low to moderate dosages. At 0.4 vol% GH, the 28-day strength rises to ≈4.4 MPa (Setup 1) and ≈3.3 MPa (Setup 2). The maximum improvement is achieved at 0.8 vol% GH, where the flexural strength peaks at ≈4.8 MPa in Setup 1 and ≈3.6 MPa in Setup 2—representing increases of roughly 20–25% relative to the biochar-only mixture. At higher fibre dosages (1.2–1.6 vol%), however, the strength declines to 3.3–3.8 MPa (Setup 1) and 2.4–2.8 MPa (Setup 2), consistent with the onset of fibre congestion and reduced matrix continuity. The ratio between the two loading configurations (≈1.25–1.35) reflects the expected anisotropy associated with the printed architecture.

These trends align closely with the established behaviour of fibre-reinforced cementitious composites. Numerous studies report that natural fibres enhance flexural strength through crack-bridging and pull-out energy dissipation, particularly when fibre length lies in the 6–15 mm range and the dosage remains below the "entanglement threshold" [65,80]. The goat-hair fibres employed here (≈8 ± 2 mm), with moderate aspect ratio and relatively high surface roughness, are well positioned to activate these mechanisms at low dosages. The initial increase in strength up to 0.8 vol% GH can be attributed to the formation of an efficient micro-reinforcing network that bridges early microcracks and delays tensile localisation. As volume fraction increases beyond this level, random alignment, overlapping fibres and local clustering create weak zones and hinder compaction—well documented causes of flexural strength reduction in natural-fibre concretes [65,80,81]. Panda et al.[82] reported that jute fibres (≈6–12 mm, ~0.5–1.0 vol.%) in extrusion-based mortars increase flexural strength at moderate contents (≈15–20%), while higher dosages reduce strength due to fibre agglomeration and porosity. Bos et al.[83] similarly showed that short cellulose-type natural fibres (~0.5–1.0 vol.%) enhance flexural behaviour of 3D printed cementitious systems (≈10–15%), whereas excessive fibre addition leads to strength reduction due to increased heterogeneity and pore connectivity.

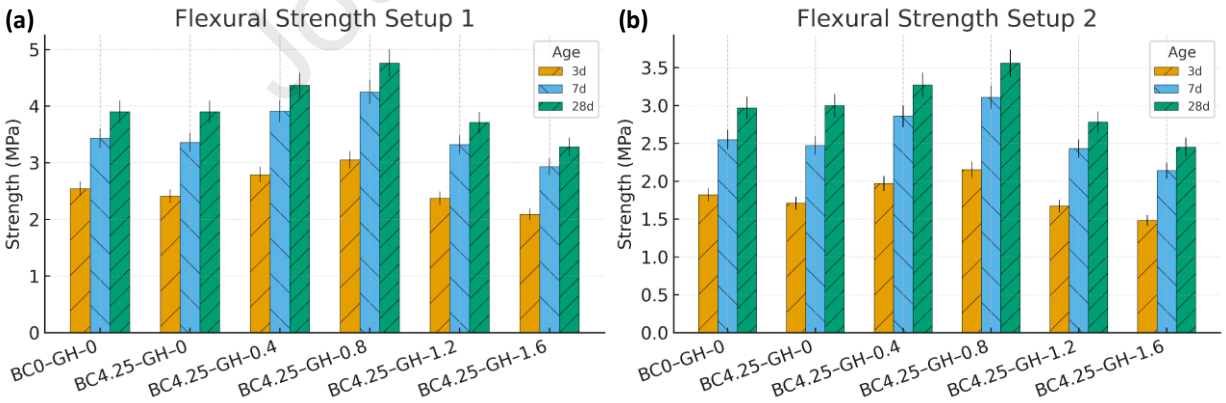

Figure 15. (a) Flexural strength of the LC³–biochar–GH mixtures under Setup 1 (loading ⊥ to printing layers) at 3, 7 and 28 days, showing the enhancement at intermediate GH contents (0.4–0.8 vol%) and the strength reduction at higher fibre volumes. (b) Corresponding flexural strength under Setup 2 (loading ∥ to printing layers), with systematically lower values but a similar ranking across mixtures, reflecting the printing-induced anisotropy of the tensile response (SD ≤ 7%).

The synergy between LC³ chemistry and fibre reinforcement further contributes to the observed behaviour. LC³ binders are known to produce denser C–A–S–H and carboaluminate networks compared with OPC, resulting in higher tensile bond strength and improved crack resistance [84]. When combined with biochar, which enhances interfacial friction and micro-mechanical interlocking, and with short GH fibres capable

of effective pull-out, the system exhibits a balanced enhancement in post-peak behaviour. Even in the declining region (1.2–1.6 vol% GH), flexural capacity remains comparable to typical values reported for other natural-fibre mortars (2.5–4.0 MPa) [65,80,81] , confirming that the LC³–biochar matrix maintains structural integrity despite increased heterogeneity at high fibre contents.

From a construction standpoint, these flexural results—together with the compressive strength and elastic modulus values reported earlier—demonstrate that the LC³–biochar–GH composites meet the mechanical requirements for non-structural and semi-structural 3D-printed components. The increased flexural capacity at 0.4–0.8 vol% GH directly improves interlayer bridging, surface toughness, and resistance to filament-edge cracking during handling and service [3]. At the same time, the compressive strengths (30–34 MPa in Setup 1 and 18–24 MPa in Setup 2) and elastic moduli (13–22 GPa) lie well within the ranges reported for practical 3D-printed mortars used in load-bearing walls, façade panels and modular infill structures [4]. Consequently, the optimised mixture BC4.25-GH-0.8 provides a favourable balance between rheological and mechanical performance, making it an attractive candidate for field-scale additive construction applications. The Herschel–Bulkley yield stress (~639 Pa) lies within an optimal intermediate-to-high range, ensuring adequate shape stability and buildability, while the plastic viscosity (~6.4 Pa·s) remains among the lower values, facilitating pumpability and extrusion. Mechanically, this mixture exhibits the highest flexural strength, indicating effective crack-bridging, while the compressive strength remains within an acceptable structural range despite a moderate reduction. Accordingly, 0.8 vol.% GH provides the best balance between printability-related rheological behaviour and mechanical performance.

3.3. Durability Assessment

3.3.1. Effect of elevated temperatures on compressive strength

The results of this section has been presented in Appendix A.

3.3.2. Durability performance under combined acid–chloride exposure

The results of this section has been presented in Appendix A.

3.4. Self-sensing behaviour under cyclic loading

3.4.1. Experimental cyclic piezoresistive response

For the cyclic piezoresistive tests, two mixtures were selected to represent the bounds of self-sensing performance in the LC³–biochar–GH samples. The biochar-only composite BC4.25–GH-0 was chosen as a benchmark to isolate the effect of the conductive LC³–biochar matrix without fibre bridging, while BC4.25–GH-0.8 represents the optimised formulation identified previously in terms of mechanical performance.

Two stress levels were adopted, 30% and 60% of the ultimate compressive strength of Setup 1 (≈9 MPa and ≈18 MPa, respectively), to probe both service-like and damage-enhancing regimes. The lower level corresponds to a quasi-linear, subcritical range where microcracking is limited and the response is dominated by reversible elastic deformation, which is representative of normal operating loads in 3D-printed structures. The higher level approaches the onset of non-linear damage while remaining safely

765 below failure, thereby promoting cumulative stiffness degradation and allowing the electromechanical
766 response to be interrogated under progressive microcrack evolution.

767 Figure 16 presents the coupled strain–FCR response of BC4.25–GH-0 under 50 cycles of sinusoidal
768 loading at 0.25 Hz. The full records Figure 16a, Figure 16c) show highly periodic strain histories, with
769 peak strains of ≈0.05% at 30% loading and ≈0.10–0.11% at 60% loading, accompanied by synchronous,
770 polarity-reversed oscillations in the fractional change in resistivity |FCR|. The |FCR| amplitude is ≈5–6%
771 at 30% loading and increases to ≈12–13% at 60% loading. On this basis, the effective gauge factor GF =
772 $(\Delta R/R_0)/\varepsilon$ is of the order of ≈90 at 30% loading and ≈115 at 60% loading. These values are two orders of
773 magnitude higher than those of conventional metallic strain gauges (GF ≈ 2) and are comparable to many
774 carbon-based cementitious sensors reported in the literature [85,86], underscoring the strong
775 electromechanical sensitivity of the LC^3–biochar matrix even in the absence of conductive nanofillers.
776 Graphene-based and graphene nanoplatlet (GNP)-based cement composites tested under cyclic
777 compression commonly exhibit GF values of 50–200 at filler contents of 3–5 wt.% [87–90], while carefully
778 dispersed CNT or CNT/GNP hybrids in cementitious matrices have been shown to reach GF ≈ 100–200 at
779 total nanocarbon dosages around 0.5–1.0 vol.% [24,91].

780 The magnified 10-cycle windows (Figure 16b, Figure 16d) reveal stable, repeatable electromechanical
781 loops with negligible drift over time, indicating that the conductive network formed by biochar particles
782 and the LC^3 binder remains structurally robust under repeated loading. The anti-phase relationship between
783 strain and |FCR|—with resistivity decreasing during compression—reflects a percolation-controlled
784 conduction mechanism: densification under load reduces inter-particle spacing and increases contact
785 points, thereby enhancing charge transport. This behaviour is consistent with prior observations in carbon-
786 black- and CNT-modified cementitious composites, where compression induces a reversible reduction in
787 electrical resistivity through contact and tunnelling effects [85,86].

788 Figure 17 characterises damage evolution via a cycle-by-cycle Damage Index derived from the
789 instantaneous elastic modulus. The instantaneous elastic modulus ($E_{(inst)}$) was obtained directly from the
790 stress–strain record at each time step, using the ratio σ/ε after converting strain values from percent to
791 fractional form. To avoid numerical artefacts, extremely small strains were replaced by a safe threshold
792 and all negative or non-physical modulus values were discarded. The resulting $E_{(inst)}$ series was then
793 smoothed and used as the stiffness-based indicator for subsequent analysis.

794 The Damage Index was computed through a lightweight, script-based post-processing routine that
795 combines four independent cyclic indicators: (i) degradation of instantaneous stiffness relative to the initial
796 cycles; (ii) drift in the peak–valley envelope of the FCR response; (iii) evolution of the FCR–strain
797 hysteresis area; and (iv) cumulative fatigue accumulation over the cycling history. Each indicator was
798 normalised to [0,1] and averaged to yield a single scalar measure that increases monotonically with damage
799 severity. This compact formulation captures the major fatigue- and microcracking-related mechanisms
800 typically reported for cementitious and composite self-sensing materials, while remaining robust against
801 measurement noise and cycle-to-cycle variability.

As shown in Figure 17, at 50% loading, the Damage Index increases gradually from ≈0.05 to ≈0.34 over the 50 cycles, indicating moderate microcrack nucleation and limited stiffness degradation. At 80% loading, damage accumulates more rapidly and stabilises at ≈0.05–0.38, consistent with enhanced interfacial debonding, frictional sliding and progressive disruption of the LC^3 gel network. The Damage-Index–FCR correlation (Figure 17c) shows that low damage states correspond to a broad |FCR| envelope, whereas higher damage levels collapse onto a narrower |FCR| band. This suggests that as microcracking localises, the conduction network becomes increasingly governed by a reduced number of dominant pathways, leading to a more constrained and damage-controlled electromechanical response.

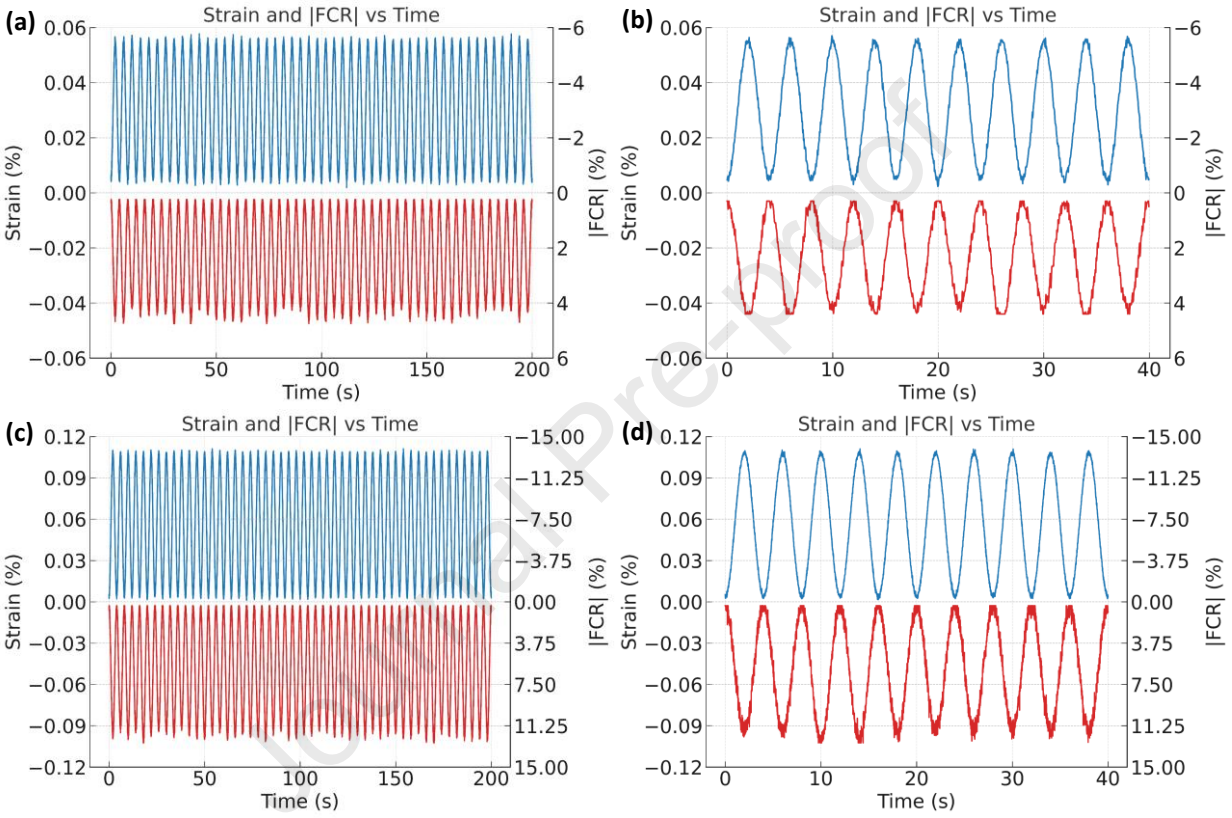

Figure 16. Coupled strain and fractional change in resistivity (|FCR|) of BC4.25–GH-0 under cyclic compression: (a) full 50-cycle record at 30% ultimate strength; (b) magnified 10-cycle segment at 30% loading; (c) full 50-cycle record at 60% loading; (d) magnified 10-cycle segment at 60% loading.

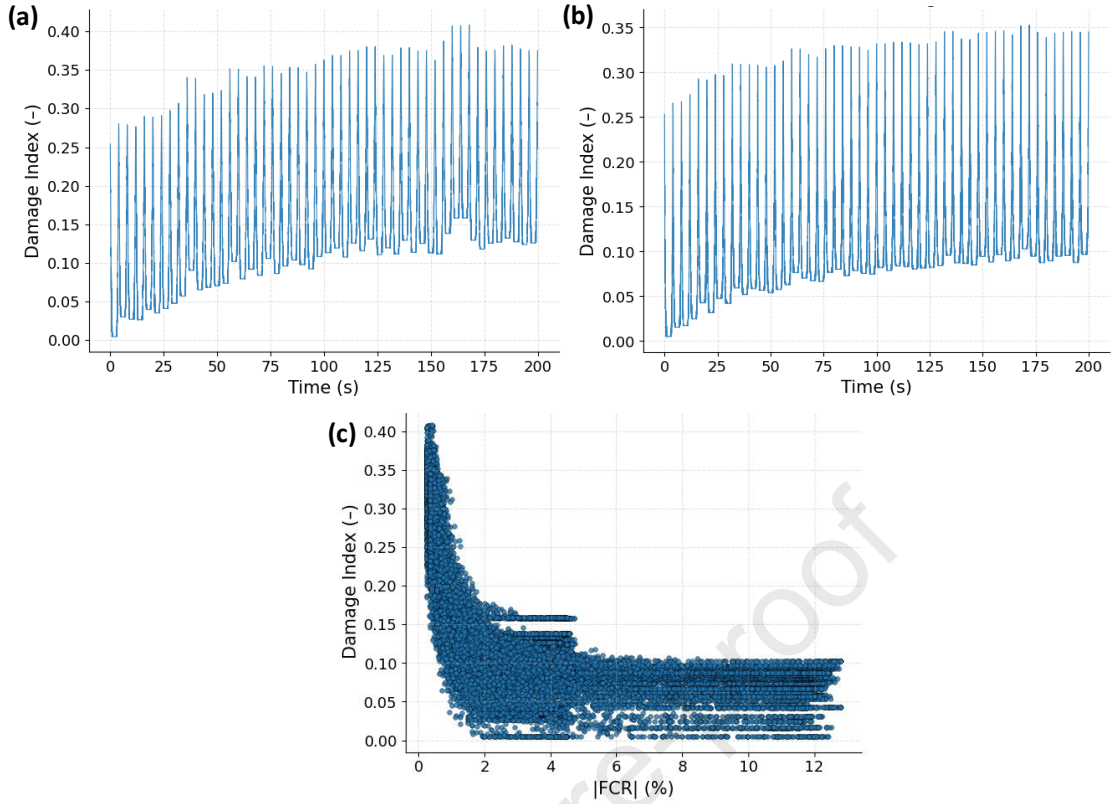

Figure 17. Damage Index of BC4.25–GH-0: (a) Damage Index vs time at 80% loading; (b) Damage Index vs time at 50% loading; (c) correlation between Damage Index and |FCR| for all cycles.

Figure 18 shows the cyclic electromechanical response of BC4.25–GH-0.8 at 30% and 60% of its ultimate compressive strength. Owing to its lower elastic modulus and optimised microstructure and fibre content, BC4.25–GH-0.8 exhibits noticeably higher strain amplitudes and substantially larger resistivity fluctuations than BC4.25–GH-0, while preserving excellent cyclic stability.

Under 30% loading (Figure 18a and Figure 18b), the specimen develops peak cyclic strains of ≈0.06–0.07%, compared with ≈0.05% in the fibre-free benchmark. The associated fractional change in resistivity |FCR| reaches ≈6–8%, representing a ≈30–40% enhancement in electromechanical sensitivity relative to BC4.25–GH-0. This enhancement originates from the combined action of (i) improved LC^3–biochar percolation connectivity and (ii) mechanical interlocking and crack-bridging provided by the goat-hair fibres, which modulate the conductive pathways during loading. The effective gauge factor of BC4.25–GH-0.8 lies in the range ≈110 at 30% loading—higher than the benchmark mixture and within the upper bound of carbon-based cementitious sensors reported in the literature, where typical GF values range between 50 and 200 for GNP-, CNT-, or graphene-modified cements at 0.5–5 wt.% filler content [85,86].

At 60% loading (Figure 18c and Figure 18d), the peak strain increases to ≈0.10–0.12%, with |FCR| reaching ≈15–18%. The gauge factor stabilises in the range ≈130, confirming a stress-dependent electromechanical amplification consistent with the progressive activation of fibre-controlled microcrack mechanisms. Notably, despite the higher stress level, BC4.25–GH-0.8 maintains clean, repeatable loops with no visible drift over the full 50 cycles, demonstrating that fibre bridging and increased percolation density do not destabilise the conductive network. Instead, they enable more pronounced and reversible changes in

resistivity under compression, a feature desirable for high-resolution self-monitoring in 3D-printed structural elements.

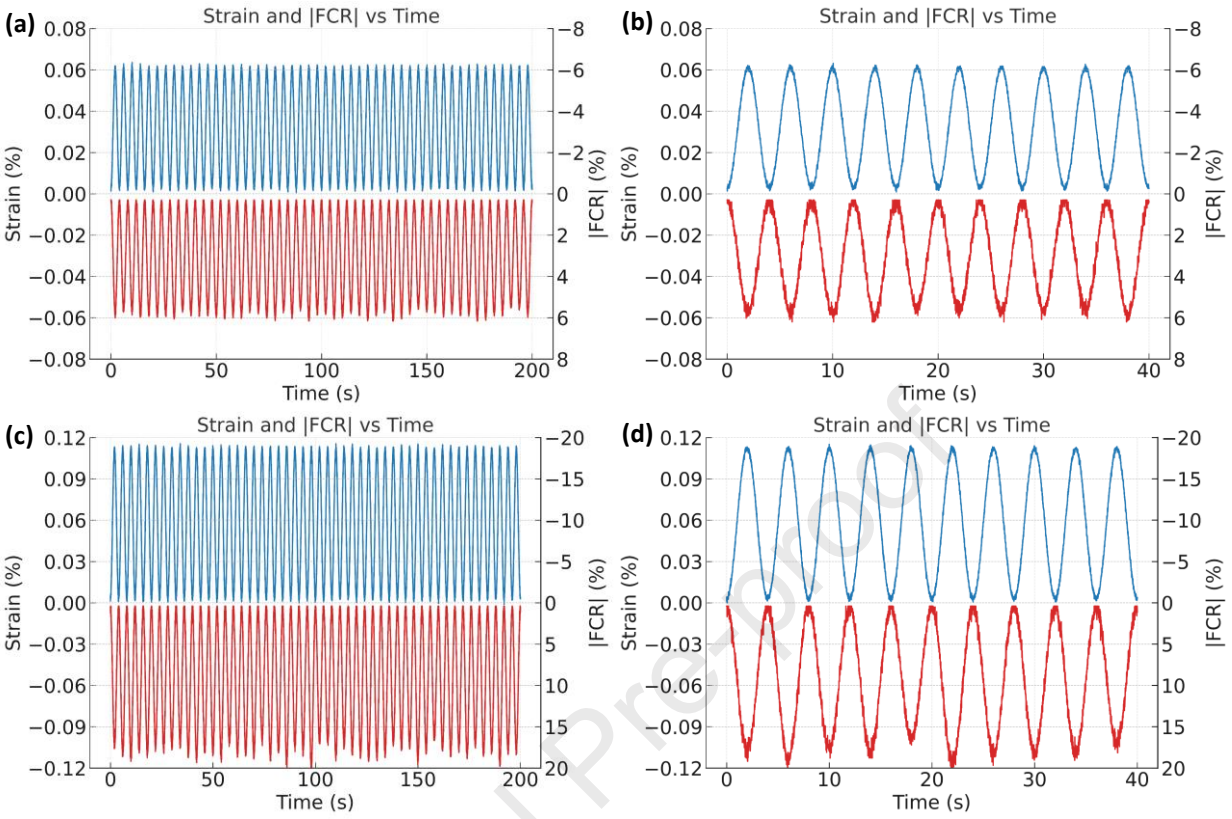

Figure 18. Coupled strain and fractional change in resistivity (|FCR|) of BC4.25–GH-0.8 under cyclic compression: (a) full 50-cycle record at 30% ultimate strength; (b) magnified 10-cycle segment at 30% loading; (c) full 50-cycle record at 60% loading; (d) magnified 10-cycle segment at 60% loading.

Figure 19 characterises the corresponding Damage Index evolution. At 50% loading (Figure 19a), the Damage Index gradually increases from ≈0.03 to ≈0.30–0.32, indicating modest stiffness degradation and stable crack evolution. Relative to BC4.25–GH-0, the damage accumulation curve for BC4.25–GH-0.8 is slightly flatter, suggesting that fibre reinforcement improves fatigue resistance and delays stiffness decay—consistent with well-documented roles of natural fibres in suppressing crack opening and controlling microcrack coalescence [81]. Under 80% loading (Figure 19b), the Damage Index stabilises around ≈0.02–0.35, lower than or comparable to the benchmark mixture despite the substantially larger FCR amplitudes. This indicates that the enhanced electromechanical sensitivity of BC4.25–GH-0.8 does not arise from severe microstructural deterioration; rather, it emerges from controlled crack-modulated changes in conductive pathways.

The Damage Index–FCR map (Figure 19c) exhibits a characteristic narrowing of |FCR| scatter at higher damage states, similar to the behaviour observed for the benchmark mixture. However, the convergence occurs at higher |FCR| values for BC4.25–GH-0.8 (≈12–18%), reflecting the stronger coupling between mechanical degradation and conductive pathway rearrangement when fibres are present. This behaviour is consistent with prior observations in fibre-reinforced and carbon-modified cementitious sensors, where

fibre bridging leads to concentrated conduction through fewer dominant pathways as microcracks stabilise [92].

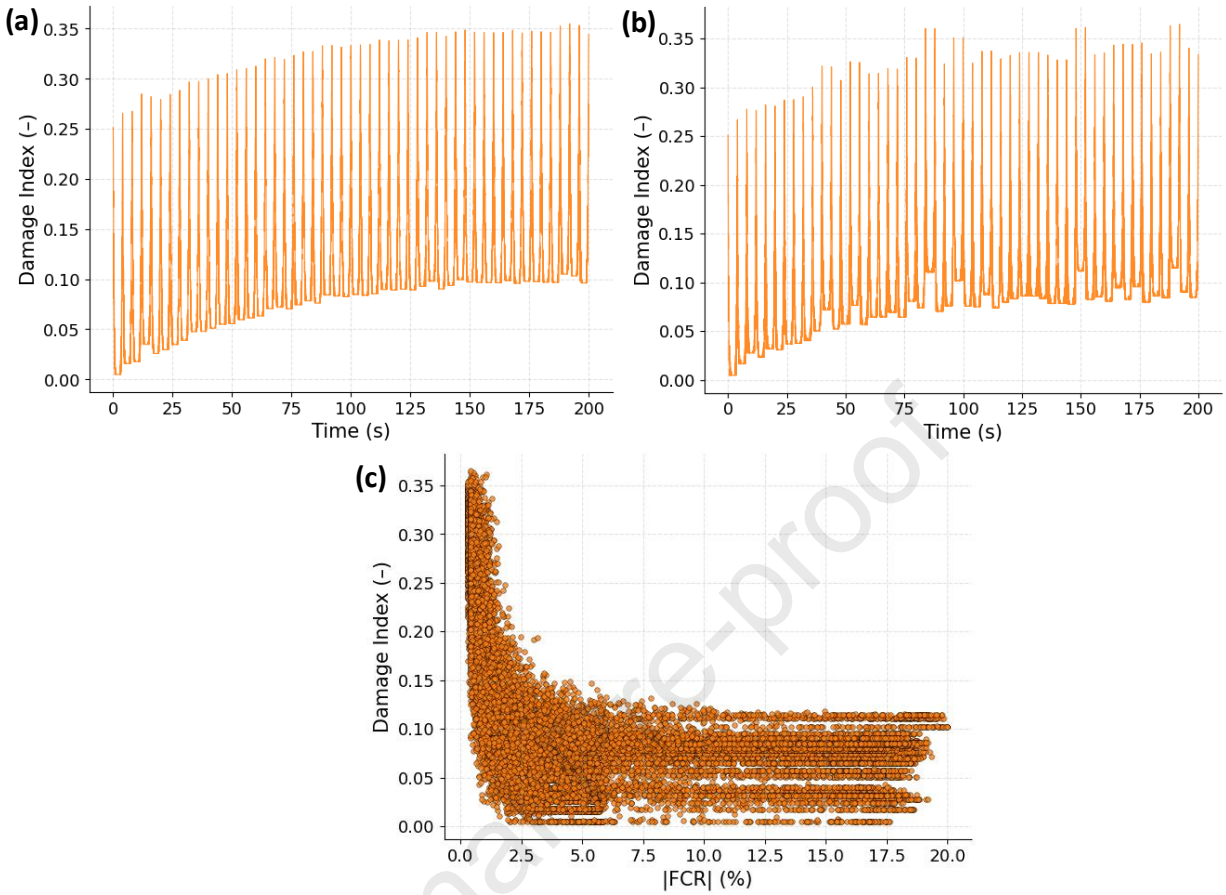

Figure 19. Damage Index of BC4.25–GH-0.8 during cyclic loading: (a) Damage Index vs time at 80% loading; (b) Damage Index vs time at 50% loading; (c) correlation between Damage Index and |FCR| for all cycles.

Indeed, the cyclic response confirms that BC4.25–GH-0.8 provides a significantly stronger and more tunable piezoresistive behaviour than BC4.25–GH-0, while simultaneously demonstrating reduced damage accumulation. This dual improvement—higher sensitivity and enhanced mechanical integrity—positions the optimised mixture as a robust candidate for integrated self-sensing in 3D-printed LC³-based structural components.

3.4.2. Machine-learning framework for multi-output self-sensing prediction

3.4.2.1. Random Forest multi-output regression

The cyclic electromechanical dataset generated from the LC³–biochar–GH composites provides a uniquely challenging learning problem due to its multi-scale coupling between instantaneous deformation, electrical resistivity change, stiffness evolution, and damage accumulation. To capture these relationships in a unified predictive framework, two supervised learning models—a Random Forest multi-output regressor and an XGBoost multi-output ensemble was trained using all four response variables—stress, strain, E_inst, and Damage Index—allowing the model to exploit shared information across targets and account for the intrinsic physical correlations embedded in the time-resolved data.

Unlike conventional single-output regressions, the multi-output structure is particularly well suited to this material system because each predicted quantity is fundamentally linked to the others. Stress and strain form the primary mechanical pair, but their relationship is not purely elastic under cyclic loading: the instantaneous modulus E_inst evolves cycle-by-cycle based on stiffness loss and nonlinear compliance. Similarly, the Damage Index is a composite metric constructed from stiffness degradation, drift in FCR hysteresis, hysteresis energy variation, and cumulative fatigue progression. These components make the dataset strongly hierarchical and path-dependent—characteristics that decision-tree ensembles are naturally capable of learning because they partition the feature space along nonlinear thresholds that correspond closely to mechanical state changes during cycling.

Figure 20 shows the actual–predicted relationships obtained from the Random Forest model. Stress and strain predictions exhibit extremely tight alignment with the 1:1 diagonal, demonstrating that the algorithm successfully resolved both the high-frequency oscillatory behaviour and the low-frequency trends associated with gradual damage accumulation. The ability to reproduce strain—despite its very narrow dynamic range (0–0.12%) and sensitivity to measurement noise—indicates that the model captured fine-scale geometric distortions encoded in the cyclic waveform. Stress, which directly scales with strain but is modulated by the time-varying modulus, is predicted with similarly high fidelity, confirming that the multi-output structure allowed the model to internalise the coupled mechanical–damage interactions.

Predictions for instantaneous modulus E_inst show moderate scatter, which is expected given its definition as σ/ε at each time step. Very small strain increments near turning points amplify numerical sensitivity, producing physically meaningful variability that is inherently more difficult to learn. Nevertheless, the predicted E_inst values follow the correct trajectory and preserve the cycle-by-cycle stiffness decay pattern, indicating that the Random Forest captured the dominant microstructural signatures associated with modulus degradation. The Damage Index, despite being an aggregated nonlinear descriptor, is also reproduced with strong consistency. The model accurately tracks the progressive increase in damage with cycle number as well as the transient oscillations associated with hysteresis shape, demonstrating that it effectively recognised the multicomponent structure of the index (stiffness loss, drift, hysteresis energy, and cumulative fatigue).

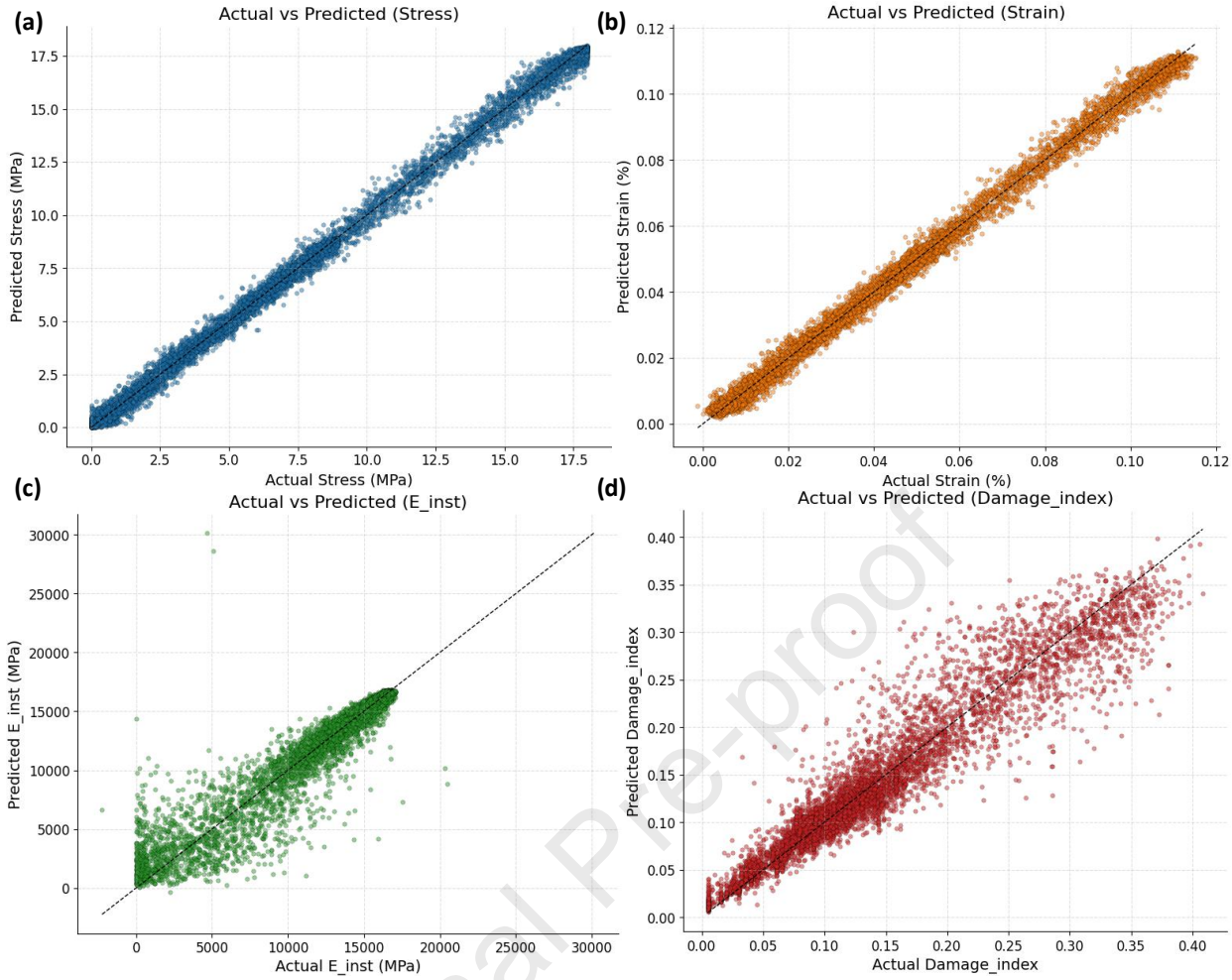

Figure 20. Comparison between measured and model-predicted values for the four sensing-related outputs: (a) compressive stress; (b) strain; (c) instantaneous modulus (E_inst); and (d) Damage Index.

Residual distributions (Figure 21) further support the robustness of the model. Stress and strain errors follow near-symmetric Gaussian-like histograms centred at zero, indicating that there is no systematic bias in predicting either the elastic backbone or the periodic fluctuations. The residuals for E_inst exhibit a broader tail, aligning with the known numerical sensitivity of the modulus at low strain amplitudes; however, the central peak remains sharp and unbiased. The Damage Index residuals remain narrow and well-distributed, confirming that both local cyclic features and global fatigue trends were captured accurately.

The 5-fold cross-validation results show outstanding generalisation performance. Stress and strain maintain R^2 values above 0.99 across all folds, while E_inst and Damage Index—despite their more complex and noise-sensitive definitions—show R^2 values in the 0.90–0.93 range. This level of performance is noteworthy because the model is required to learn not only smooth mechanical relationships but also abrupt transitions in stiffness, subtle shifts in resistivity-driven sensing behaviour, and cumulative microdamage effects embedded within thousands of time steps.

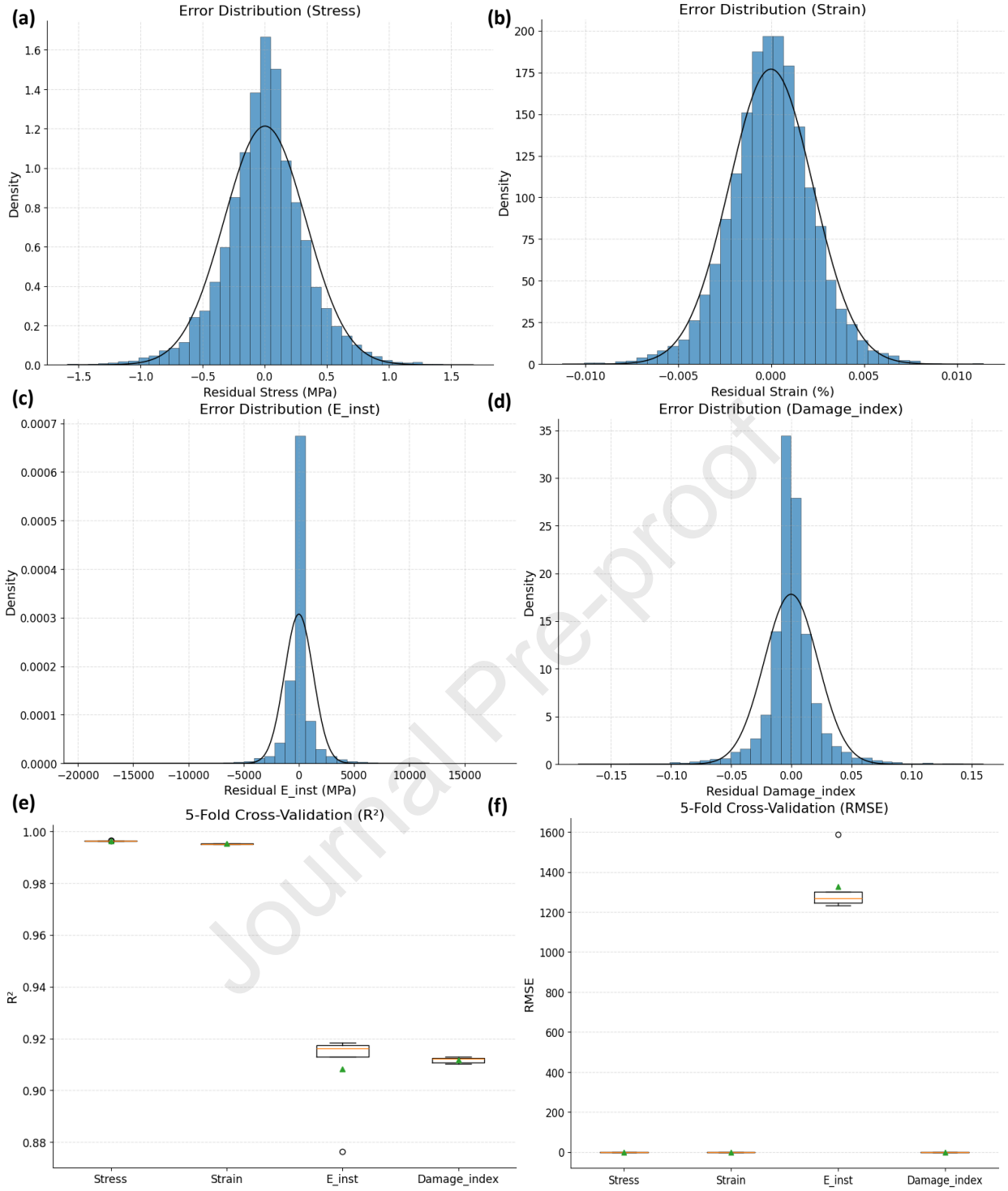

Figure 21. Residual errors and 5-fold cross-validation performance of the Random Forest multi-output model: (a) residual stress; (b) residual strain; (c) residual instantaneous modulus; (d) residual Damage Index (e) distribution of R^2 across five validation folds; (f) distribution of RMSE across five validation folds.

3.4.2.2. XGBoost multi-output regression

Figure 22 illustrates the predictive performance of the XGBoost multi-output regression model for the four target variables—stress, strain, instantaneous modulus, and Damage Index—using the full cyclic sensing dataset. The Actual–Predicted relationships exhibit near-perfect alignment for stress and strain, with regression lines closely overlapping the 1:1 diagonal, confirming an outstanding generalisation capacity across the complete range of mechanical and electromechanical responses. The predicted stress values

reproduce the experimental trajectory with a coefficient of determination of R^2 = 0.9964, while strain predictions achieve R^2 = 0.9954, matching the fidelity required for high-resolution structural sensing applications.

More importantly, the XGBoost model demonstrates superior capability in capturing the nonlinear, history-dependent variables (E_inst and Damage Index) both of which encode evolving microstructural behaviour under cyclic loading. As shown in Figure 22c and Figure 22d, the model successfully tracks the broad distribution of these parameters despite their intrinsic scatter, achieving R^2 = 0.9269 for E_inst and R^2 = 0.9286 for Damage Index. These gains over the Random Forest model can be attributed to XGBoost's tree-boosting architecture, which constructs sequential learners that explicitly correct the residual error of previous trees. Such a structure is particularly effective for the heterogeneous patterns embedded in E_inst, which depends on instantaneous σ–ε ratios, and in Damage Index, which incorporates cycle-dependent stiffness loss, hysteresis drift, and cumulative fatigue contributions.

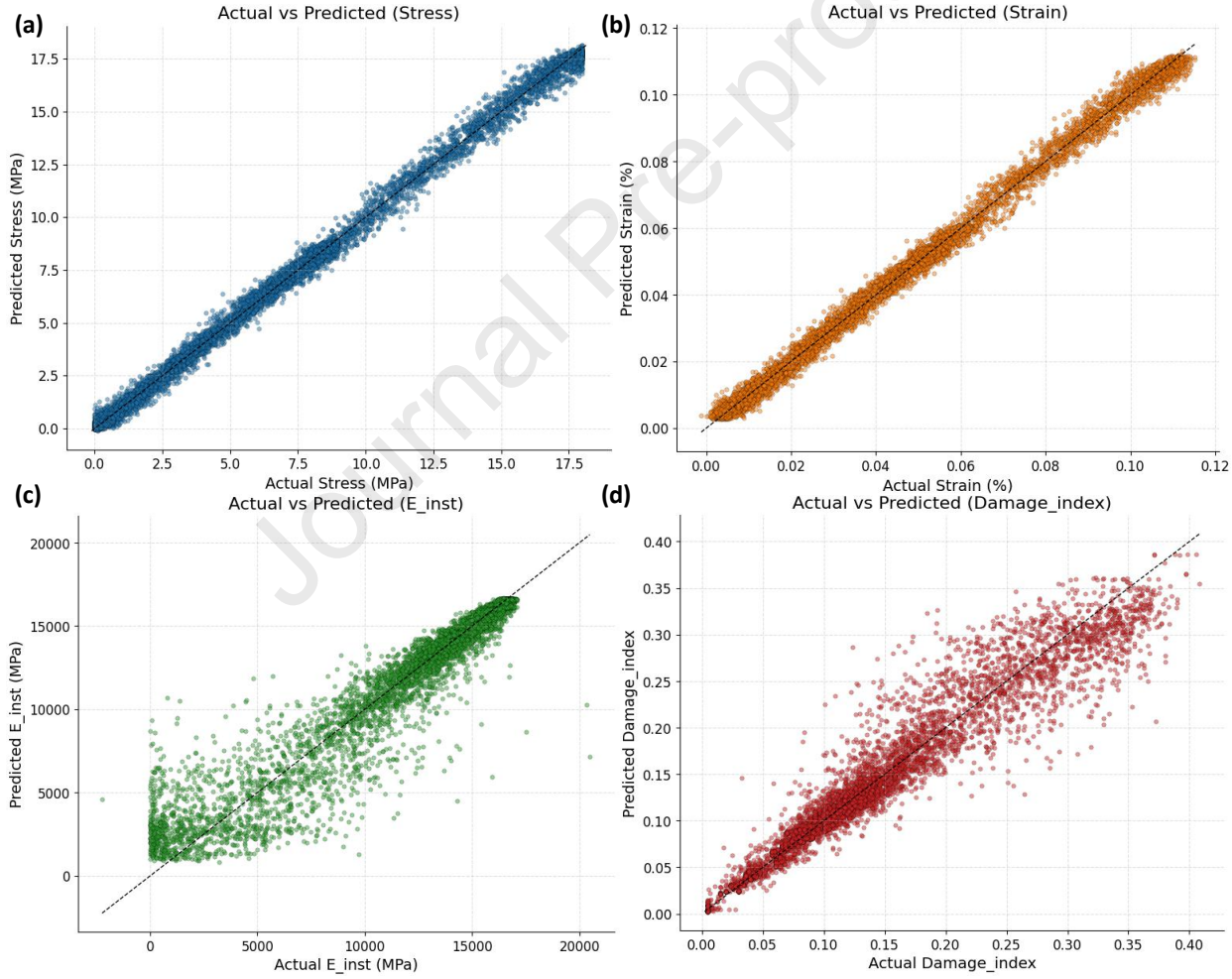

Figure 22. Comparison between measured and model-predicted values for the four sensing-related outputs using the XGBoost multi-output model: (a) compressive stress; (b) strain; (c) instantaneous modulus (E_inst); (d) Damage Index.

The error-distribution plots in Figure 23 further reinforce these observations. Residuals for stress and strain are tightly centred around zero and follow near-Gaussian distributions, indicating unbiased predictions and stable variance across the entire dataset. For E_inst and Damage Index, the error histograms show slightly broader—but still symmetric—profiles, consistent with the higher physical variability of these quantities.

Importantly, XGBoost suppresses the heavy-tail behaviour observed in the Random Forest residuals, demonstrating more effective control over extreme deviations.

Cross-validation performance, summarised in Figure 23e and Figure 23f, confirms the robustness of the model. The 5-fold R^2 values remain consistently high with minimal fold-to-fold fluctuation—particularly for Damage Index and E_inst—indicating that the boosted trees capture the underlying electromechanical patterns in a generalisable manner rather than memorising specific segments of the cyclic waveform. The corresponding RMSE distributions remain narrow and stable, reflecting the model's resilience to variations in loading amplitude, cycle history, and strain-rate fluctuations.

From a practical standpoint, these results hold significant implications for integrating self-sensing LC^3–biochar–GH composites into digital-construction and structural-health-monitoring frameworks. The ability to predict not only primary mechanical variables (stress, strain) but also microstructural degradation indicators (E_inst and Damage Index) with high fidelity suggests that boosted-tree models can serve as reliable digital twins for printed cementitious elements, enabling real-time condition assessment and predictive maintenance.

A quantitative comparison between the two developed models highlights these trends. While both methods deliver exceptional performance for stress and strain, XGBoost provides noticeable improvements for E_inst (R^2 from 0.91 → 0.93) and Damage Index (R^2 from 0.91 → 0.93), and simultaneously reduces the RMSE for both variables (from 1298 → 1193 MPa and 0.0224 → 0.0202). These enhancements underscore the suitability of gradient-boosted frameworks for capturing the subtle, multiscale electromechanical signatures arising from cyclic loading in mineral-based conductive composites.

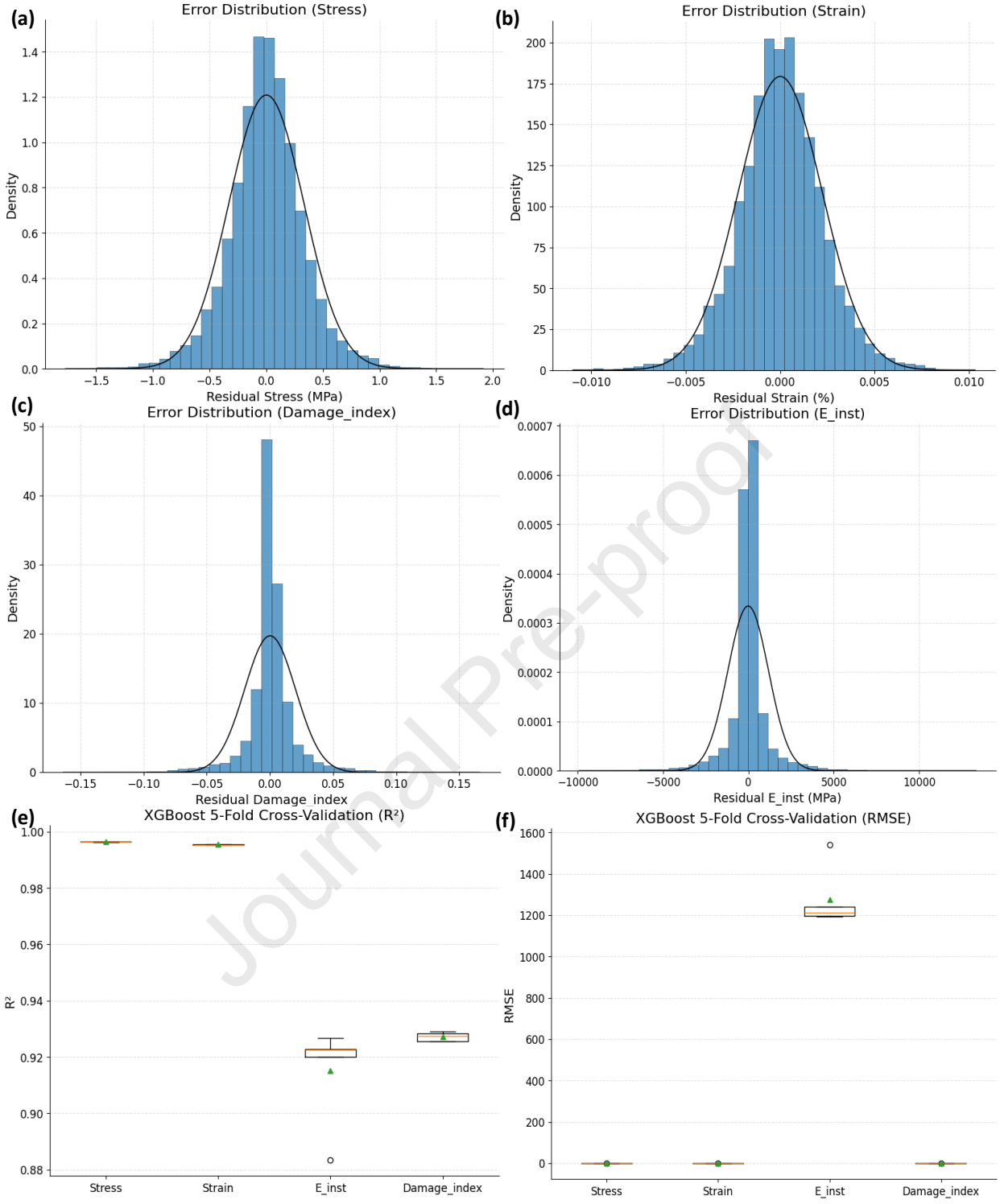

Figure 23. Residual errors and 5-fold cross-validation performance of the XGBoost multi-output model: (a) residual stress; (b) residual strain; (c) residual Damage Index; (d) residual instantaneous modulus; (e) distribution of R^2 across five validation folds; (f) distribution of RMSE across five validation folds.

Feature importance analysis (Figure 24) shows that |FCR| is the dominant predictor in both XGBoost and Random Forest models, accounting for the majority of the predictive power, while specimen identifiers contribute only marginally. This confirms that the model primarily relies on the intrinsic electromechanical sensing signal rather than specimen-specific variability. The consistent trend across both models supports the robustness of the proposed minimal-input framework and demonstrates that the mechanical–damage

state can be reliably inferred directly from |FCR| without requiring additional loading or time-dependent information.

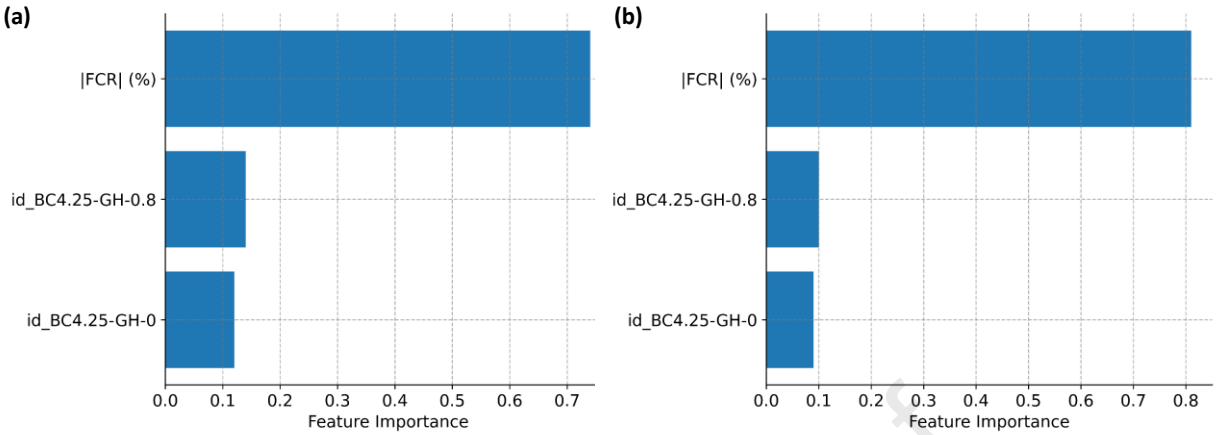

Figure 24. Feature importance of the input variables for (a) XGBoost and (b) Random Forest models, showing the dominant contribution of |FCR| compared to specimen identifiers.

From a practical standpoint, the observed differences between the Random Forest and XGBoost models have direct implications for real-world structural health monitoring applications. The Random Forest model is generally associated with stable predictive behaviour and lower sensitivity to overfitting due to its ensemble averaging structure, making it particularly suitable for continuous monitoring scenarios [5]. In addition, its relatively simple architecture and lower sensitivity to hyperparameter tuning make it computationally efficient and easier to implement in practical systems [4].

In contrast, the XGBoost model demonstrates a higher sensitivity to nonlinear interactions and subtle damage evolution, making it more effective for capturing progressive degradation and complex electromechanical behaviour [3]. However, this improved sensitivity is typically accompanied by increased model complexity, higher computational demand, and greater dependency on parameter tuning due to its sequential boosting framework [5]. Therefore, while Random Forest provides stable and computationally efficient predictions for continuous monitoring, XGBoost offers enhanced capability for detailed damage assessment and high-resolution analysis.

3.5. CO_2 Uptake and Electromechanical Response of LC^3–Biochar Composites

The CO_2 uptake behaviour of the LC^3–biochar–GH composites follows a multilayered adsorption–reaction process that integrates physical sorption, ion-driven electrical responses, and progressive microstructural carbonation of the binder. As illustrated in Figure 25, all samples exhibit a rapid initial sorption stage during the first 5–7 days, followed by a gradual deceleration toward a quasi-steady plateau across the 30-day exposure period. This biphasic evolution is consistent with the behaviour reported for CO_2-reactive cementitious adsorbents [93–97], where early uptake is dominated by the availability of high-surface-area carbonaceous phases, while later-stage adsorption is progressively controlled by diffusion resistance and the depletion of reactive sites.

This biphasic uptake profile in both BC4.25–GH-0 and BC4.25–GH-0.8 reflects the coexistence of two distinct CO_2-binding mechanisms within the LC^3–biochar–GH matrix. The early-stage uptake is dominated

by reversible physisorption on biochar micropores and on the internal surfaces of partially open LC³ hydration products, which is fully recoverable during low-temperature regeneration. In contrast, the slower long-term tail corresponds to the progressive formation of stable carbonate phases—primarily $CaCO_3$ from portlandite and carboaluminate species from the LC³ alumina content—which are irreversible under mild regeneration conditions (60 °C). This dual mechanism explains both the rapid initial mass gain and the incomplete capacity recovery observed across adsorption cycles, as only the physisorbed fraction participates in reversible cycling, whereas the chemically bound carbonate fraction accumulates permanently within the microstructure.

For reference, the LC³-control mixture without biochar (BC0-GH-0) exhibits a significantly lower CO_2 uptake (≈260 g/m²), confirming that the enhanced capture capacity in the biochar-containing composites primarily originates from the carbonaceous phase rather than the cementitious matrix alone. The biochar-only composite (GH-0) reaches ≈1000 g/m² in the first cycle, systematically outperforming the fibre-reinforced GH-0.8, a trend that aligns with the well-documented effect of carbon-rich microstructures in enhancing CO_2 sorption through both micropore filling and surface functional groups such as carboxyl, phenolic and lactonic moieties [84,93,98–101].

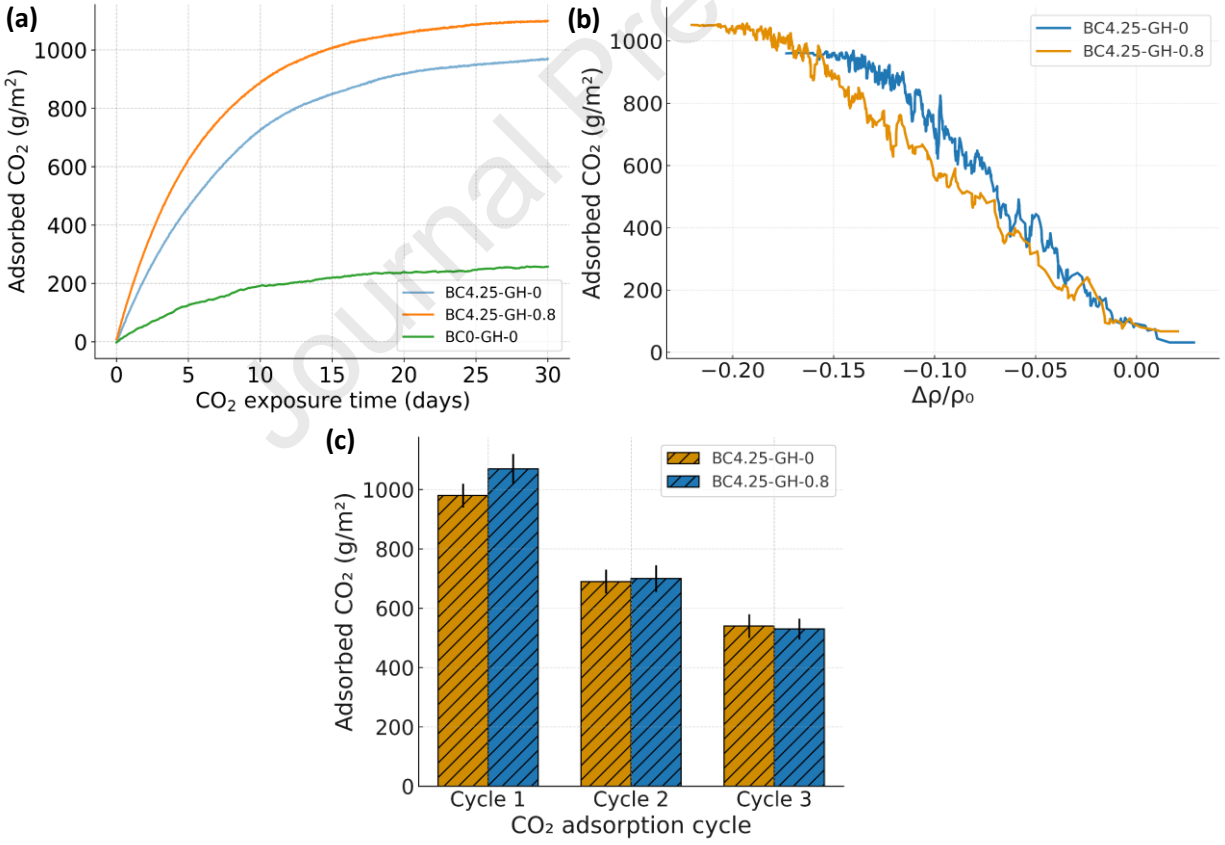

Figure 25. CO_2 uptake and electrical response of LC³–biochar composites under continuous flow conditions:(a) breakthrough curves showing outlet CO_2 concentration over 30 days for BC4.25–GH-0 and BC4.25–GH-0.8; (b) normalised electrical resistivity change ($\Delta\rho/\rho_0$) during CO_2 exposure; (c) cumulative CO_2 uptake across three consecutive adsorptions–regeneration cycles for both composites.

The higher uptake of GH-0 reflects its more open and interconnected pore structure, where biochar particles create a broad distribution of micro- and mesopores that support multilayer physisorption and accelerate

CO_2 access to the LC^3 binder [34]. In contrast, the presence of goat-hair fibres in GH-0.8 partially occupies percolation channels, reducing accessible sorption volume and intensifying localised LC^3 gel densification during early carbonation. Similar pore-blocking effects have been noted in fibre-modified cementitious systems, including flax-, PVA- and basalt-reinforced carbons [102,103]. Beyond physisorption, chemisorption also plays a critical role: as CO_2 diffuses into the LC^3 matrix, portlandite and aluminate-containing phases react to form $CaCO_3$, Na_2CO_3 and hemicarbonate species, densifying the C–A–S–H gel and progressively decreasing internal porosity. This mechanistic transformation has been extensively documented in LC^3 materials subjected to high CO_2 concentrations [84,99–101], and explains the observed slowdown phase in both composites.

The electrical response recorded through $\Delta\rho/\rho_0$ (Figure 25b) closely mirrors the mass-based uptake curves, with both materials exhibiting negative resistivity changes during CO_2 ingress. This characteristic signal arises because carbonation alters the ionic landscape of porewater, enriching it with HCO_3^- and CO_3^{2-} and lowering the resistivity of the liquid phase [93]. Simultaneously, densification of the LC^3 matrix and the reduction of interparticle spacing within the biochar network increase the number of conductive pathways [33,104]. The GH-0 composite shows a more pronounced resistivity decrease, directly reflecting its higher sorption capacity and more continuous carbon-based percolation network—a behaviour also reported in carbon-black and CNT-modified binders undergoing accelerated carbonation [105–107].

The multi-cycle adsorption results (Figure 25c) reveal a predictable decline in sorption capacity with each regeneration cycle: GH-0 retains ≈70% of its initial capacity in Cycle 2 and ≈55% in Cycle 3, while GH-0.8 stabilises at approximately 65% and 50%, respectively. This loss in uptake capability is characteristic of cementitious and hybrid carbonaceous adsorbents [84,97,99], where a combination of irreversible chemisorption, microstructural densification and partial pore collapse reduces the number of available adsorption sites. The regeneration procedure applied here (60°C for 48 h) is sufficient to remove physisorbed CO_2 and physically retained moisture, but cannot reverse $CaCO_3$ formation, nor restore clogged micropores in fibre-containing systems [93,108]. The slightly sharper decline in GH-0.8 emphasises the dual role of fibres: while mechanically beneficial, they tend to accumulate bound water and accelerate carbonation around their interfaces, both of which hinder pore reactivation upon thermal regeneration.

When compared with CO_2-sorbing materials commonly used in the built environment, the performance of the LC^3–biochar composites stands out. Portland cement and traditional OPC-rich mortars typically exhibit CO_2 uptakes in the range of 200–450 g/m² [84,100,108], primarily through limited $Ca(OH)_2$ carbonation. A consolidated comparison with major classes of CO_2-sorbing construction materials is presented in Table 5. LC^3 systems improve this range to roughly 300–700 g/m² due to the presence of reactive aluminates [101]. Carbon-enriched cementitious composites—activated carbon, carbon black, CNT or GNP reinforced systems—can reach 800–1500 g/m² depending on pore structure and carbon loading [105–108]. Lime-based materials, including aerial lime ($CaO \rightarrow Ca(OH)_2$) and hydraulic lime mortars (NHL), can achieve high CO_2 uptake through recarbonation of $Ca(OH)_2$ back to $CaCO_3$; however, their overall sorption rate is

slower, strongly humidity-dependent, and limited by their relatively low mechanical integrity in structural settings [93,109–111]. In comparison, GH-0 with ≈1000 g/m² positions itself among the higher-performing carbonaceous sorbents while maintaining the mechanical and durability advantages of LC³. GH-0.8, despite lower uptake, still meets the performance range needed for functional sorption in composite structural materials.

Table 5. Comparison of CO_2 uptake performance of the LC³–biochar composites (BC4.25–GH-0 and BC4.25–GH-0.8) with representative cementitious, carbon-based and lime-based sorbents reported in the literature.

Material System	Dominant Mechanism	Typical CO_2 Uptake (g/m²)	Notes / Literature Trends
BC4.25–GH-0 (This study)	Physisorption (biochar micropores) + LC³ carbonation + ionic conductive path densification	≈1000 (Cycle 1); 700 (Cycle 2); 550 (Cycle 3)	Highest uptake among tested materials; strong $\Delta\rho/\rho_0$ correlation
BC4.25–GH-0.8 (This study)	Mixed sorption + pore blocking via fibres	≈900 (Cycle 1); 600 (Cycle 2); 500 (Cycle 3)	Fibre network reduces available pore volume & regeneration efficiency
Portland cement paste (OPC)	$Ca(OH)_2$ carbonation	200–450	Slow uptake; humidity-dependent; limited reactive sites [33,112]
LC³ mortar (no carbon additives)	Carbonation of portlandite + carboaluminate formation	300–700	Higher uptake than OPC due to aluminates [93,108,113]
Activated carbon–cement composite	Physisorption + multilayer adsorption	800–1500	High surface area; rapid early uptake [93,114]
Carbon black / GNP / CNT cement composites	High-surface-area adsorption + conductive network	900–1500	Uptake depends on carbon loading (1–5 wt.%) [33,104]
Lime mortar (CL / NHL)	$Ca(OH)_2 \rightleftarrows CaCO_3$ recarbonation	600–1100 (depending on porosity & humidity)	High ultimate uptake but slow kinetics; strong RH sensitivity [93,115,116]
Pure calcium hydroxide (lab-scale)	Direct $CO_2 \rightarrow CaCO_3$	up to 4500	Not structurally applicable; idealized upper bound [117]

The combined CO_2 uptake and electrical response also underscore the functional duality of these materials. The strong correlation between q(t) and $\Delta\rho/\rho_0$ indicates that the composite not only captures CO_2 but also internally senses its own sorption state through measurable electrical signatures—a highly attractive feature for applications involving continuous monitoring or self-regulating environments. While such applications are beyond the scope of the present study, the mechanistic and performance evidence strongly supports this direction from a materials science standpoint.

3.6. Microstructural analysis

3.6.1. Thermogravimetric analysis

The results of this section has been presented in Appendix A.

3.6.2. Mercury Intrusion Porosimetry (MIP): Pore Size Distribution

The results of this section has been presented in Appendix A.

3.7. Embodied CO_2 Assessment

A simplified cradle-to-gate CO_2 assessment was performed to quantify the reduction in embodied CO_2 achieved by replacing 40 % of OPC with the optimized LC³ blend. The functional unit was 1 t of dry binder, and the system boundary was limited to raw-material extraction, calcination or milling, and

grinding/blending up to the factory gate. To ensure a fair comparison, all external conditions were kept identical for the reference and LC³ binders: OPC production was assumed to be domestic (no imported cement), and identical transport distances and logistics were applied to all constituents. This streamlined calculation follows the principles of ISO 14040/44 [118] but considers only CO_2 emissions; no other greenhouse gases or impact categories were evaluated. The optimized LC^3 binder contains 60 % calcined kaolinite, 5 % calcined illite, 5 % calcined montmorillonite, and 30 % ground limestone, replacing 40 % of OPC by mass. To isolate the specific impact of clinker substitution, all other constituents held constant in both mixes (e.g., SP and VMA) were excluded from the comparison. Cradle-to-gate CO_2 emissions (t CO_2 t^{-1} binder) were calculated in a transparent spreadsheet using:

$$CO_2 = \frac{1}{1000}\sum_i m_i \times EF_i \quad \text{(Eq. 4)}$$

where m_i is the mass of constituent i (kg per tonne of binder) and EF_i is its cradle-to-gate CO_2 emission factor (kg CO_2 kg^{-1}). Emission factors were taken from peer-reviewed sources: OPC = 0.84 ± 0.05 kg CO_2 kg^{-1} [119,120], calcined clay = 0.37 ± 0.05 kg CO_2 kg^{-1} [6,121], ground limestone = 0.05 ± 0.02 kg CO_2 kg^{-1} [122]. In this study, a conservative emission factor of 0.05 kg CO_2 kg^{-1} was adopted to avoid assuming negative emissions, following recommendations from recent biochar LCA reviews [123]. Using these values, a conventional binder composed of 100 % OPC yields an embodied CO_2 of ≈0.92 t CO_2 t^{-1} binder, in line with previous cement LCA benchmarks. For the optimised LC³ binder employed in this study—containing 60 % OPC and 40 % LC³ (itself composed of 60 % calcined kaolinite, 5 % calcined illite, 5 % calcined montmorillonite and 30 % ground limestone)—the corresponding value decreases to ≈0.69 t CO_2 t^{-1} binder. This reduction of about 0.23 t CO_2 t^{-1} (≈25 % saving) arises directly from the lower emission factors of calcined clay and limestone relative to clinker, and is fully consistent with earlier reports that LC³ formulations with 30–50 % clinker substitution can reduce cradle-to-gate CO_2 by 20–40 % [122,124]. Although a detailed techno-economic analysis is beyond the scope of this study, numerous investigations have reported that substituting clinker with locally available LC^3 can reduce total binder costs by roughly 10–30 %, with the potential for even greater savings at higher replacement levels [6,124,125].

The LC³–biochar binders used in the BC4.25–GH-0 and BC4.25–GH-0.8 mixtures further include 4.25 wt.% biochar relative to the cementitious binder (OPC+LC³). For the optimized LC³–biochar binder, the embodied CO_2 reduced to 0.68–0.71 t CO_2 t^{-1} compared to 100 % OPC.

The contribution of goat-hair fibres to embodied CO_2 is comparatively minor. Direct LCA data for goat hair are scarce, but studies on analogous keratin-based fibres (wool, mohair) report cradle-to-gate footprints in the range of roughly 5–15 kg CO_2-eq kg^{-1} fibre when emissions are appropriately allocated between meat and fibre co-products [21,126]. Given that the maximum fibre dosage in this study is only 0.8 vol.% (i.e., well below 1 wt.% of the composite), even an upper-bound emission factor would modify the binder-level embodied CO_2 by less than a few percent. For clarity, the quantitative results reported here therefore neglect the fibre contribution, while recognising that a detailed sensitivity analysis could be added in future work without altering the main conclusions.

A comparison with lime-based binders further highlights the environmental positioning of the LC³–biochar system. Cradle-to-gate studies on hydrated lime and natural hydraulic lime mortars typically indicate embodied CO_2 values on the order of 0.85–1.1 t CO_2 t^{-1} binder, reflecting the decarbonation of limestone and the energy intensity of lime kilns [127,128]. Although lime mortars can partially recover CO_2 through recarbonation during service life, this uptake falls outside the cradle-to-gate system boundary considered here. On this basis, the LC³–biochar binders BC4.25–GH-0 and BC4.25–GH-0.8 achieves approximately 25 % lower embodied CO_2 than a 100 % OPC binder and roughly 15–30 % lower values than typical lime mortars, while simultaneously providing enhanced mechanical performance, superior durability against thermal and chemical exposures, and additional functionalities such as piezoresistive self-sensing and active CO_2 uptake. This combination of reduced embodied emissions and multifunctional behaviour underscores the potential of LC³–biochar composites as structurally efficient and environmentally intensive alternatives to both Portland cement and traditional lime-based systems in future low-carbon construction.

4. Conclusion

This study introduced a sustainable, locally sourced multifunctional 3D-printed LC³ composite—combining natural animal-hair fibres and activated biochar—to achieve structural performance, self-sensing capability, and CO_2 uptake. The mixtures used a fixed 40% LC³ replacement and 4.25 wt% biochar, with 0–1.6% goat-hair fibre volumes. The experimental programme included rheological evaluation (flow-curve and stress-growth), mechanical testing in both orientations, durability under elevated temperatures (300–500 °C) and acid–chloride exposure, and microstructural analyses (SEM, TGA/DTG, and mercury intrusion porosimetry). Multifunctional behaviour was assessed through cyclic piezoresistive loading (30% and 60% of compressive strength), combined with machine-learning prediction of stress, strain, modulus, and a damage index. CO_2 uptake was measured using a controlled micro-chamber system, and regeneration was verified over repeated cycles. The principal findings are summarised as follows:

- Yield stress increased from 452 to 741 Pa (1.6% GH) and τ_peak from ≈720 to ≈1000 Pa, while viscosity decreased from 17.9 → 6.2 Pa·s with biochar and moderate GH. BC4.25–GH0.8 achieved the optimal τ_0–μ_p balance for extrusion. Higher GH (>0.8%) may require increased pump pressure and stricter flow control due to fibre flocculation.
- Compressive strength remained 30–34 MPa (Setup 1) and 18–24 MPa (Setup 2) with anisotropy 1.3–1.4; flexural strength peaked at 4.8 MPa (⊥) and 3.6 MPa (∥) at 0.8% GH, while modulus decreased from ≈22 to ≈11 GPa. Fibres are effective up to ≈0.8%, beyond which congestion weakens the matrix; controlled dispersion is essential to prevent layer instability.
- Strength retention at 300 °C was ≈76–79% (GH ≤ 0.8%) and ≈63–68% (≥1.2% GH); at 500 °C it declined to ≈38–52% and ≈34–38%, respectively. After 120-day NaCl–HCl exposure, loss was ≈20% (reference), ≈23–26% (≤0.8% GH), and ≈30–34% (>0.8%). LC³–biochar shows strong durability, though high fibre contents should be limited in aggressive environments.

- Cyclic loading (30% and 60% f_c) of the optimal mixture (BC4.25–GH0.8) produced stable FCR with increasing amplitude and clear hysteresis. Both Random Forest and XGBoost achieved high accuracy in predicting stress and strain; however, XGBoost showed superior performance for E_inst and damage index, reflecting improved capability in capturing nonlinear and degradation-related behaviour. Trends followed stiffness degradation. Reliable sensing requires proper electrode layout, percolation continuity, and moisture control.
- BC4.25–GH0 reached ≈1000 g/m² CO_2 uptake (Cycle 1) and BC4.25–GH0.8 ≈900 g/m², exceeding OPC (~450 g/m²) and approaching lime (~1100 g/m²). After regeneration (60 °C, 48 h), capacities stabilised at ≈700/550 and ≈600/500 g/m². $\Delta\rho/\rho_0$ tracked uptake, confirming detectability. Overall, LC^3–biochar composites show potential for passive indoor CO_2 buffering, provided humidity, airflow, and regeneration intervals are appropriately controlled.

5. Limitations and Strategic Research Outlook

Although the multifunctional potential of the LC^3–biochar composite developed in this study provides a strong foundation for net-zero and sustainable digital construction using natural and locally sourced materials, several limitations define the current boundary of applicability and offer opportunities for future research. The rheological behaviour was evaluated under controlled laboratory extrusion conditions; scaling to full-scale pumping and continuous printing requires quantifying pump-pressure demands, flow instabilities, and the operational limits imposed by fibre dispersion. The mechanical response was examined using small-scale printed elements, and future work should address structural-scale anisotropy, interlayer slip, and long-term fatigue under realistic service loads. The durability assessment focused on elevated-temperature and acid–chloride environments; broader evaluations under cyclic wetting–drying, freezing–thawing, and carbonation ageing are needed to establish lifecycle robustness. While stable performance was observed within the investigated timeframe, the long-term behaviour of keratin-based fibres remains time-dependent and may evolve under extended exposure. Further investigation of fibre–matrix interface stability over longer durations is therefore recommended. The self-sensing behaviour was validated under controlled cyclic loading, whereas practical deployment will require stable electrode configuration, moisture compensation, and long-term drift correction. The CO_2-uptake performance was demonstrated at the material scale; translating this capability into functional indoor-buffering systems demands a deeper understanding of sorption kinetics under variable humidity and airflow, regeneration efficiency, and system-level design constraints. While the present study evaluates mechanical performance, self-sensing behaviour, and CO_2 uptake individually, their coupled interaction under service conditions involves more complex mechanisms. Mechanical loading can induce microcrack formation, altering conductive pathways and pore connectivity, which may either enhance or degrade sensing response and CO_2 transport depending on the damage state. Conversely, CO_2 uptake processes may change pore connectivity and internal structure, leading to either beneficial or adverse effects on both mechanical and electrical performance. A rigorous evaluation of these coupled effects requires advanced methodologies,

such as in-situ chemo–mechanical testing (simultaneous loading under controlled CO_2 exposure), stepwise load–unload self-calibration protocols for tracking baseline drift in electrical response, and multi-physics or data-driven frameworks (e.g., hybrid physics-informed machine learning or SHAP-based feature attribution) to decouple the contributions of damage evolution and adsorption processes. These aspects are beyond the scope of the present study and are identified as a key direction for future research. Together, these directions outline a strategic research path toward the practical, large-scale deployment of multifunctional LC^3–biochar composites in next-generation sustainable construction.

6. Acknowledgement

The authors acknowledge the support provided by His Majesty Trust Fund (HMTF) and Sultan Qaboos University with the reference numbers “SR/ENG/CAED/23/01”.

7. Conflicts of interest

The author has no conflicts of interest to declare.

8. Data Availability Statement

Requests for all types of data used to support the findings of this study, after the publication of this article, will be considered by the corresponding author, subject to obtaining permission from the owners.

9. Ethics statement

This study does not contain any studies involving human or animal participants.

10. Declaration of generative AI and AI-assisted technologies in the writing process

During the preparation of this work, the authors used Grammarly to improve language and readability. After using this tool/service, the authors reviewed and edited the content as needed and take full responsibility for the content of the publication.

References

[1] S. Michalopoulos, Printable Profile of Sustainable Modified Cementitious Materials for Additive Manufacturing Applications in Digital Construction, (2020).

[2] M. Abedi, M.B. Waris, M.K. Al-Alawi, K.S. Al-Jabri, A.H. Al-Saidy, From local earth to modern structures: A critical review of 3D printed cement composites for sustainable and efficient construction, J. Build. Eng. 100 (2025) 111638. https://doi.org/https://doi.org/10.1016/j.jobe.2024.111638.

[3] M. Abedi, M.B. Waris, M. Al-Alawi, K. Al-Jabri, M. Rezazadeh, Data-Driven design of sustainable LC^3 for 3D printing with Omani clays, Results Eng. 28 (2025) 108061. https://doi.org/https://doi.org/10.1016/j.rineng.2025.108061.

[4] M. Abedi, M.B. Waris, M. Al-Alawi, K. Al-Jabri, Next-Generation Net-Zero Composite for Underwater 3D Printing Construction: Hybrid Machine Learning Optimized LC3 with Recycled Rubber, J. Mater. Res. Technol. (2025). https://doi.org/https://doi.org/10.1016/j.jmrt.2025.10.084.

[5] M. Abedi, M.B. Waris, M. Al-Alawi, K. Al-Jabri, Transformative low-carbon 3D-printed infrastructure: Machine learning-driven self-sensing and self-heating limestone calcined clay

cement (LC3) composites, Constr. Build. Mater. 493 (2025) 143123.

[6] K. Scrivener, F. Martirena, S. Bishnoi, S. Maity, Calcined clay limestone cements (LC3), Cem. Concr. Res. 114 (2018) 49–56.

[7] H. Khan, J. Ahmad, S. Irfan, Multi objective optimization of novel ultra-green high performance LC3 concrete incorporating geopolymer cold-bonded lightweight artificial aggregates using central composite design based response surface methodology, Case Stud. Constr. Mater. 23 (2025) e05589. https://doi.org/https://doi.org/10.1016/j.cscm.2025.e05589.

[8] S.S. Khedkar, S.D. Khodke, D.A. Bhand, G.S. Khamkar, S.M. Gunjal, Mechanical Performance of LC3 Concrete Incorporating Fine Rubber Aggregates, in: J. Phys. Conf. Ser., IOP Publishing, 2025: p. 12004.

[9] W. Dong, A.H. Ahmed, M. Liebscher, H. Li, Y. Guo, B. Pang, M. Adresi, W. Li, V. Mechtcherine, Electrical resistivity and self-sensing properties of low-cement limestone calcined clay cement (LC3) mortar, Mater. Des. 252 (2025) 113790.

[10] W. Dong, S. Peng, K. Wang, Y. Huang, L. Shi, F. Wu, W. Li, Integrated triboelectric self-powering and piezoresistive self-sensing cementitious composites for intelligent civil infrastructure, Nano Energy. 135 (2025) 110656.

[11] H. Li, J. Yang, L. Wang, L. Li, Y. Xia, T. Köberle, W. Dong, N. Zhang, B. Yang, V. Mechtcherine, Multiscale assessment of performance of limestone calcined clay cement (LC3) reinforced with virgin and recycled carbon fibers, Constr. Build. Mater. 406 (2023) 133228.

[12] B. Hopkins, W. Si, M. Khan, C. McNally, Recent Advancements in Polypropylene Fibre-Reinforced 3D-Printed Concrete: Insights into Mix Ratios, Testing Procedures, and Material Behaviour, J. Compos. Sci. 9 (2025) 292.

[13] B. Nematollahi, P. Vijay, J. Sanjayan, A. Nazari, M. Xia, V. Naidu Nerella, V. Mechtcherine, Effect of polypropylene fibre addition on properties of geopolymers made by 3D printing for digital construction, Materials (Basel). 11 (2018) 2352.

[14] A. Ramezani, S. Modaresi, P. Dashti, M.R. GivKashi, F. Moodi, A.A. Ramezanianpour, Effects of different types of fibers on fresh and hardened properties of cement and geopolymer-based 3D printed mixtures: a review, Buildings. 13 (2023) 945.

[15] H. Varela, G. Barluenga, M. Sonebi, Evaluation of basalt fibers and nanoclays to enhance extrudability and buildability of 3D-printing mortars, J. Build. Eng. 97 (2024) 110776.

[16] J. Sun, F. Aslani, J. Lu, L. Wang, Y. Huang, G. Ma, Fibre-reinforced lightweight engineered cementitious composites for 3D concrete printing, Ceram. Int. 47 (2021) 27107–27121.

[17] H. Li, J. Wei, K.H. Khayat, 3D Printing of Fiber-Reinforced Calcined Clay-Limestone-Based Cementitious Materials: From Mixture Design to Printability Evaluation, Buildings. 14 (2024) 1666.

[18] S. Eyupoglu, Sustainable plant-based natural fibers, in: Sustain. Text. Appar. Ind. Sourc. Nat. Raw Mater., Springer, 2020: pp. 27–48.

[19] S. Luhar, T. Suntharalingam, S. Navaratnam, I. Luhar, J. Thamboo, K. Poologanathan, P. Gatheeshgar, Sustainable and renewable bio-based natural fibres and its application for 3D printed concrete: A review, Sustainability. 12 (2020) 10485.

[20] G.D.S. Cornish, Exploitation of biomaterials in construction: keratin feather fibres in cement-based materials, (2025).

[21] N. Hassas, F. Omidi Moaf, M. Kurpińska, T. Bardzińska-Bonenberg, J. Borucka, H.S. Abdelgader, R. Soman, M. Miśkiewicz, The impact of goat hair as a natural animal fiber on properties of the lightweight cement composite, Sci. Rep. 15 (2025) 6943.

[22] F.C. Antico, P. Rojas, F. Briones, G. Araya-Letelier, Animal fibers as water reservoirs for internal curing of mortars and their limits caused by fiber clustering, Constr. Build. Mater. 267 (2021) 120918.

[23] J.A. Alomaja, A.A. Jimoh, O.P. Joseph, U.N. Wilson, Flexural and tensile properties of chemically treated guinea corn husk-cow hair hybrid fiber reinforced cement composite, Mater. Today Proc. 86 (2023) 77–81.

[24] M. Abedi, K. Al-Jabri, B. Han, R. Fangueiro, P.B. Lourenço, A.G. Correia, Advancing infrastructure resilience: A polymeric composite reinforcement grid with self-sensing and self-

heating capabilities, Constr. Build. Mater. 435 (2024) 136730. https://doi.org/https://doi.org/10.1016/j.conbuildmat.2024.136730.

[25] M. Abedi, F. Gulisano, B. Han, R. Fangueiro, A.G. Correia, The pioneer of intelligent and sustainable construction in tunnel shotcrete applications: a comprehensive experimental and numerical study on a self-sensing and self-heating green cement-based composite, Meas. Sci. Technol. 35 (2024) 65601.

[26] M. Abedi, R. Fangueiro, A. Gomes Correia, A review of intrinsic self-sensing cementitious composites and prospects for their application in transport infrastructures, Constr. Build. Mater. 310 (2021). https://doi.org/10.1016/j.conbuildmat.2021.125139.

[27] M. Abedi, R. Fangueiro, A. Camões, A. Gomes Correia, Evaluation of CNT/GNP's synergic effects on the Mechanical, Microstructural, and durability properties of a cementitious composite by the novel dispersion method, Constr. Build. Mater. 260 (2020) 120486. https://doi.org/https://doi.org/10.1016/j.conbuildmat.2020.120486.

[28] M. Abedi, O. Hassanshahi, J.A.O. Barros, A. Gomes Correia, R. Fangueiro, Three-Dimensional Braided Composites as Innovative Smart Structural Reinforcements, Compos. Struct. (2022) 115912. https://doi.org/10.1016/j.compstruct.2022.115912.

[29] M.I. Haque, R.I. Khan, W. Ashraf, H. Pendse, Production of sustainable, low-permeable and self-sensing cementitious composites using biochar, Sustain. Mater. Technol. 28 (2021) e00279.

[30] C. Zhang, X. Zhu, M. Li, Y. Zhang, Y. Zhang, N. Banthia, H. Ye, D.C.W. Tsang, Enhancing interface adhesion of 3D printable concrete by biochar integration, Cem. Concr. Compos. (2025) 106383.

[31] L. Wang, V.N. Nerella, D. Li, Y. Zhang, B. Ma, E. Ivaniuk, J. Zhang, X. Zhu, J. Yan, V. Mechtcherine, Biochar-augmented climate-positive 3D printable concrete, Commun. Mater. 5 (2024) 257.

[32] Z. Kang, J. Zhang, N. Li, Y. Yang, T. Lv, J. Lu, Development of self-sensing cement composites by incorporating hybrid biochar and nano carbon black, Cem. Concr. Compos. 153 (2024) 105708.

[33] Z. Yang, J. Xu, T. Chen, X. Gao, L. Qin, Internal and external synergistic CO2 capture of cement-based materials using modified biochar, Constr. Build. Mater. 470 (2025) 140696.

[34] G. Mishra, P.A. Danoglidis, S.P. Shah, M.S. Konsta-Gdoutos, Carbon capture and storage potential of biochar-enriched cementitious systems, Cem. Concr. Compos. 140 (2023) 105078.

[35] P. Sikora, P. Woliński, M. Chougan, S. Madraszewski, W. Węgrzyński, B.K. Papis, K. Federowicz, S.H. Ghaffar, D. Stephan, A systematic experimental study on biochar-cementitious composites: Towards carbon sequestration, Ind. Crops Prod. 184 (2022) 115103.

[36] S. Gupta, A. Kashani, A.H. Mahmood, T. Han, Carbon sequestration in cementitious composites using biochar and fly ash–Effect on mechanical and durability properties, Constr. Build. Mater. 291 (2021) 123363.

[37] J. Liu, L. Cheng, H. Jin, F. Xing, Sustainable utilization of concrete slurry waste in eco-friendly artificial lightweight cold-bonded aggregates: An alternative pathway for efficiently sequestrating CO2, Constr. Build. Mater. 421 (2024) 135759. https://doi.org/https://doi.org/10.1016/j.conbuildmat.2024.135759.

[38] J. Liu, M. Li, H. Jin, L. Cheng, F. Xing, The role of different ratios of biochar in the artificial lightweight cold-bonded aggregates (ALCBAs) containing high volume of red mud (RM), Constr. Build. Mater. 422 (2024) 135815. https://doi.org/https://doi.org/10.1016/j.conbuildmat.2024.135815.

[39] N. Crozet, J. Jawtusch, Camels, Goats and Horses-the most important livestock species in Oman, Sustain. Land-and Resour. Use between Tradit. Mod. (2007) 100.

[40] B. Abu-Jdayil, M.S. Barkhad, A.-H.I. Mourad, M.Z. Iqbal, Date palm wood waste-based composites for green thermal insulation boards, J. Build. Eng. 43 (2021) 103224.

[41] S.A. Abdul-Wahab, Y. Charabi, R. Al-Maamari, G.A. Al-Rawas, A. Gastli, K. Chan, CO2 greenhouse emissions in Oman over the last forty-two years, Renew. Sustain. Energy Rev. 52 (2015) 1702–1712.

[42] H. Bera, Y.F. Abbasi, F.F. Yoke, P.M. Seng, B.B. Kakoti, S.K.M. Ahmmed, P. Bhatnagar,

Ziprasidone-loaded arabic gum modified montmorillonite-tailor-made pectin based gastroretentive composites, Int. J. Biol. Macromol. 129 (2019) 552–563.

[43] S. Martins Torres, V. Estolano de Lima, P. de Azevedo Basto, N.T. de Araújo Júnior, A.A. de Melo Neto, Assessing the pozzolanic activity of sugarcane bagasse ash using X-ray diffraction, Constr. Build. Mater. 264 (2020) 120684. https://doi.org/https://doi.org/10.1016/j.conbuildmat.2020.120684.

[44] M.L. Elias, G. Cultrone, On the use of sodium chloride and calcined diatomite sludge as additives to improve the engineering properties of bricks made with a clay earth from Jun (Granada, Spain), Minerals. 9 (2019) 64.

[45] R. Yan, F. Meng, G. Ke, K. Jia, Comparative evaluation of the applicability of 3D printing mortar with different waste powders, Constr. Build. Mater. 443 (2024) 137825.

[46] M. Abedi, R. Fangueiro, A. Camões, A. Gomes Correia, Evaluation of CNT/GNP's synergic effects on the Mechanical, Microstructural, and durability properties of a cementitious composite by the novel dispersion method, Constr. Build. Mater. 260 (2020) 120486. https://doi.org/10.1016/j.conbuildmat.2020.120486.

[47] M. Abedi, O. Hassanshahi, A. Rashiddel, H. Ashtari, M. Seddik Meddah, D. Dias, M.A. Arjomand, K. Keong Choong, A sustainable cementitious composite reinforced with natural fibers: An experimental and numerical study, Constr. Build. Mater. 378 (2023) 131093. https://doi.org/https://doi.org/10.1016/j.conbuildmat.2023.131093.

[48] Y. Chen, S. He, Y. Zhang, Z. Wan, O. Çopuroğlu, E. Schlangen, 3D printing of calcined clay-limestone-based cementitious materials, Cem. Concr. Res. 149 (2021) 106553.

[49] W. Jin, C. Roux, C. Ouellet-Plamondon, J.-F. Caron, Life cycle assessment of limestone calcined clay concrete: Potential for low-carbon 3D printing, Sustain. Mater. Technol. 41 (2024) e01119.

[50] G.S. Mann, N. Azum, A. Khan, M.A. Rub, M.I. Hassan, K. Fatima, A.M. Asiri, Green composites based on animal fiber and their applications for a sustainable future, Polymers (Basel). 15 (2023) 601.

[51] H. Xu, Y. Huang, S. Feng, H. Jin, L. Chen, X. Chen, F. Wang, Y. Wang, Y. Zhang, L. Li, Utilization of limestone powder and silica fume as sustainable cement replacements in shotcrete: Experimental, molecular dynamics simulations, and microstructural analysis, Powder Technol. 467 (2026) 121493. https://doi.org/https://doi.org/10.1016/j.powtec.2025.121493.

[52] J. Li, N. Sheng, H. Jin, X. Liu, Y. Xu, X. Wei, T. Ngo, Strategies for upcycling multiple solid industrial waste powders: Evaluating the fresh workability, mechanical performance and sustainability of new type binders, Constr. Build. Mater. 490 (2025) 142468. https://doi.org/https://doi.org/10.1016/j.conbuildmat.2025.142468.

[53] J. Li, X. Zhu, H. Jin, M. Chen, S. Zhang, X. Wei, High value-added utilization of coal gangue power generation slag for novel alkali-activated binders: mechanical and durability evaluation, and environmental impact, Chem. Eng. J. 532 (2026) 174367. https://doi.org/https://doi.org/10.1016/j.cej.2026.174367.

[54] J. Li, Z. Yang, H. Jin, Clinker-free materials as a sustainable strategy for recycling of waste coal gangue aggregates and molybdenum tailings, Chem. Eng. J. 523 (2025) 168196. https://doi.org/https://doi.org/10.1016/j.cej.2025.168196.

[55] N. Roussel, Rheology of fresh concrete: from measurements to predictions of casting processes, Mater. Struct. 40 (2007) 1001–1012.

[56] R. Jayathilakage, P. Rajeev, J. Sanjayan, Rheometry for concrete 3D printing: a review and an experimental comparison, Buildings. 12 (2022) 1190.

[57] H. Jeong, S.-J. Han, S.-H. Choi, Y.J. Lee, S.T. Yi, K.S. Kim, Rheological property criteria for buildable 3D printing concrete, Materials (Basel). 12 (2019) 657.

[58] T.T. Le, S.A. Austin, S. Lim, R.A. Buswell, A.G.F. Gibb, T. Thorpe, Mix design and fresh properties for high-performance printing concrete, Mater. Struct. 45 (2012) 1221–1232.

[59] T. Ishida, K. Nakada, Review of rheology in cement-based materials and its application to 3D printing using concrete, Nihon Reoroji Gakkaishi. 51 (2023) 1–8.

[60] O. Canbek, Q. Xu, Y. Mei, N.R. Washburn, K.E. Kurtis, Predicting the rheology of limestone calcined clay cements (LC3): Linking composition and hydration kinetics to yield stress through

Machine Learning, Cem. Concr. Res. 160 (2022) 106925.

[61] M. Chen, L. Yang, Y. Zheng, Y. Huang, L. Li, P. Zhao, S. Wang, L. Lu, X. Cheng, Yield stress and thixotropy control of 3D-printed calcium sulfoaluminate cement composites with metakaolin related to structural build-up, Constr. Build. Mater. 252 (2020) 119090. https://doi.org/https://doi.org/10.1016/j.conbuildmat.2020.119090.

[62] J.E. Wallevik, Rheology of particle suspensions: fresh concrete, mortar and cement paste with various types of lignosulfonates, Fakultet for ingeniørvitenskap og teknologi, 2003.

[63] D. Feys, R. Verhoeven, G. De Schutter, Fresh self compacting concrete, a shear thickening material, Cem. Concr. Res. 38 (2008) 920–929.

[64] M.A.B. Beigh, C. Signorini, A. Rauf, C. Schröfl, T. Köberle, K. Grahl, T. Matschei, V. Mechtcherine, Intrinsic rheological behavior of limestone calcined clay cementitious (LC3) binders for automated construction: Effect of calcium sulfate varieties, Constr. Build. Mater. 477 (2025) 141314.

[65] L. Silvestro, A.S. Ruviaro, F.R.C. Ribeiro, P.J.P. Gleize, A.P. Kirchheim, Rheological behavior, hydration, and mechanical properties of LC3 systems with the incorporation of functionalized multi-walled carbon nanotubes, Rev. IBRACON Estruturas e Mater. 17 (2023) e17106.

[66] D. Suarez-Riera, L. Lavagna, J.F. Carvajal, J.-M. Tulliani, D. Falliano, L. Restuccia, Enhancing cement paste properties with biochar: mechanical and rheological insights, Appl. Sci. 14 (2024) 2616.

[67] S. Raghunath, M. Hoque, A.M. Gondaliya, A. Jalaee, B. Zakani, F.B. dos Santos, Q. Tu, E.J. Foster, Engineering low-carbon fiber cement with biochar: understanding its physicochemical properties and their impact on the composite performance and carbon footprint, Green Chem. 27 (2025) 9706–9723.

[68] D. Falliano, L. Restuccia, J.-M. Tulliani, G.A. Ferro, Biochar to Enhance Curing and Rheology of Mortars without Formwork., ACI Mater. J. 122 (2025).

[69] M. Rahman, S. Rawat, R. Yang, A. Mahil, Y.X. Zhang, A Comprehensive Review on Fresh and Rheological Properties of 3D Printable Cementitious Composites, J. Build. Eng. (2024) 109719.

[70] A.R. Arunothayan, B. Nematollahi, K.H. Khayat, A. Ramesh, J.G. Sanjayan, Rheological characterization of ultra-high performance concrete for 3D printing, Cem. Concr. Compos. 136 (2023) 104854.

[71] J. Liang, W. Xu, D.C.W. Tsang, Effects of various biochars on the physical, mechanical and microstructural characteristics of cement pastes and mortars: A review, Biochar-Based Cem. Concr. Sustain. Constr. (2026) 109–130.

[72] N. Roussel, Steady and transient flow behaviour of fresh cement pastes, Cem. Concr. Res. 35 (2005) 1656–1664.

[73] A. Perrot, D. Rangeard, A. Pierre, Structural built-up of cement-based materials used for 3D-printing extrusion techniques, Mater. Struct. 49 (2016) 1213–1220.

[74] Y. Weng, B. Lu, M. Li, Z. Liu, M.J. Tan, S. Qian, Empirical models to predict rheological properties of fiber reinforced cementitious composites for 3D printing, Constr. Build. Mater. 189 (2018) 676–685.

[75] V. Guerini, A. Conforti, G. Plizzari, S. Kawashima, Influence of steel and macro-synthetic fibers on concrete properties, Fibers. 6 (2018) 47.

[76] S. Room, A. Bahadori-Jahromi, Biochar-enhanced carbon-negative and sustainable cement composites: A scientometric review, Sustainability. 16 (2024) 10162.

[77] V.C. Li, On engineered cementitious composites (ECC) a review of the material and its applications, J. Adv. Concr. Technol. 1 (2003) 215–230.

[78] S. Das, M.H.R. Sobuz, V.W.Y. Tam, A.S.M. Akid, N.M. Sutan, F.M.M. Rahman, Effects of incorporating hybrid fibres on rheological and mechanical properties of fibre reinforced concrete, Constr. Build. Mater. 262 (2020) 120561.

[79] Y. Zhang, Y. Zhang, L. Yang, G. Liu, Y. Chen, S. Yu, H. Du, Hardened properties and durability of large-scale 3D printed cement-based materials, Mater. Struct. 54 (2021) 45.

[80] Z. Li, X. Zhou, H. Ma, D. Hou, Advanced concrete technology, John Wiley & Sons, 2022.

[81] M. Kurpińska, M. Pawelska-Mazur, Y. Gu, F. Kurpiński, The impact of natural fibers' characteristics on mechanical properties of the cement composites, Sci. Rep. 12 (2022) 20565.

[82] B. Panda, S.C. Paul, M.J. Tan, Anisotropic mechanical performance of 3D printed fiber reinforced sustainable construction material, Mater. Lett. 209 (2017) 146–149.

[83] F. Bos, R. Wolfs, Z. Ahmed, T. Salet, Additive manufacturing of concrete in construction: potentials and challenges of 3D concrete printing, Virtual Phys. Prototyp. 11 (2016) 209–225.

[84] F. Zunino, F. Martirena, K. Scrivener, Limestone Calcined Clay Cements (LC^3)., ACI Mater. J. 118 (2021).

[85] K. Tu, Y. Zhang, J. Wang, H. Yang, J. Tao, Q. Zeng, Synergistic Microstructures, Mechanical Properties, and Piezoresistive Performance Improvement of Nanoengineered Cementitious Composites by CNT and GNP, Buildings. 15 (2025) 4104.

[86] T. Uygunoğlu, B. Şimşek, U. Fidan, Piezoresistive and capacitive cement-based stress sensors designed by incorporating carbon nanotubes doped with graphene nanopowder for structural health monitoring, Sensors Actuators A Phys. 374 (2024) 115491.

[87] M. Abedi, R. Fangueiro, A.G. Correia, Effects of multiscale carbon-based conductive fillers on the performances of a self-sensing cementitious geocomposite, J. Build. Eng. 43 (2021) 103171. https://doi.org/https://doi.org/10.1016/j.jobe.2021.103171.

[88] M. Abedi, R. Fangueiro, A.G. Correia, Ultra-sensitive affordable cementitious composite with high mechanical and microstructural performances by hybrid CNT/GNP, Materials (Basel). 13 (2020). https://doi.org/10.3390/MA13163484.

[89] M. Abedi, R. Fangueiro, A.G. Correia, Effects of Electrodes Layout and Filler Scale on Percolation Threshold and Piezoresistivity Performances of a Cementitious-Based Geocomposite, Nanomaterials. 12 (2022) 1734. https://doi.org/10.3390/nano12101734.

[90] M. Abedi, R. Fangueiro, A.G. Correia, Development of a novel multifunctional cementitious-based geocomposite by the contribution of cnt and gnp, Nanomaterials. 11 (2021) 1–28. https://doi.org/10.3390/nano11040961.

[91] M. Abedi, R. Fangueiro, A. Gomes Correia, A review of intrinsic self-sensing cementitious composites and prospects for their application in transport infrastructures, Constr. Build. Mater. 310 (2021) 125139. https://doi.org/https://doi.org/10.1016/j.conbuildmat.2021.125139.

[92] N.G. Cotella, D.D. Gallo, K. Sapag, C.A. Barbero, D.F. Acevedo, M.M. Bruno, Peanut Shell Biochar as a Conductive Additive for Cement Composites, Waste and Biomass Valorization. 16 (2025) 2115–2124.

[93] V. Manovic, E.J. Anthony, Lime-based sorbents for high-temperature CO2 capture—a review of sorbent modification methods, Int. J. Environ. Res. Public Health. 7 (2010) 3129–3140.

[94] B. Han, X. Yu, E. Kwon, A self-sensing carbon nanotube/cement composite for traffic monitoring, Nanotechnology. 20 (2009) 445501. https://doi.org/10.1088/0957-4484/20/44/445501.

[95] M.S. Konsta-Gdoutos, P.A. Danoglidis, M.G. Falara, S.F. Nitodas, Fresh and mechanical properties, and strain sensing of nanomodified cement mortars: The effects of MWCNT aspect ratio, density and functionalization, Cem. Concr. Compos. 82 (2017) 137–151.

[96] I. Barbarin Abarzuza, 3D Porous Graphene-Polymer Materials for CO2 capture, (2022).

[97] S. Monkman, M. MacDonald, R.D. Hooton, P. Sandberg, Properties and durability of concrete produced using CO2 as an accelerating admixture, Cem. Concr. Compos. 74 (2016) 218–224.

[98] S. Gupta, J.-M. Tulliani, H.W. Kua, Carbonaceous admixtures in cementitious building materials: Effect of particle size blending on rheology, packing, early age properties and processing energy demand, Sci. Total Environ. 807 (2022) 150884.

[99] L. Wang, L. Chen, D.C.W. Tsang, B. Guo, J. Yang, Z. Shen, D. Hou, Y.S. Ok, C.S. Poon, Biochar as green additives in cement-based composites with carbon dioxide curing, J. Clean. Prod. 258 (2020) 120678.

[100] A.M. Merino-Lechuga, Á. González-Caro, E. Fernández-Ledesma, J.R. Jiménez, J.M. Fernández-Rodríguez, D. Suescum-Morales, Accelerated carbonation of vibro-compacted porous concrete for eco-friendly precast elements, Materials (Basel). 16 (2023) 2995.

[101] C.E.T. Balestra, L.R. Garcez, L.C. da Silva, M.T. Veit, E. Jubanski, A.Y. Nakano, M.H.

Pietrobelli, R. Schneider, M.A.R. Gil, Contribution to low-carbon cement studies: Effects of silica fume, fly ash, sugarcane bagasse ash and acai stone ash incorporation in quaternary blended limestone-calcined clay cement concretes, Environ. Dev. 45 (2023) 100792.

[102] G.H.D. Tonoli, U.P. Rodrigues Filho, H. Savastano Jr, J. Bras, M.N. Belgacem, F.A.R. Lahr, Cellulose modified fibres in cement based composites, Compos. Part A Appl. Sci. Manuf. 40 (2009) 2046–2053.

[103] Y. Wang, X. Jiang, S. Wang, W. Yang, W. Liu, F. Xing, K. Yang, P.A.M. Basheer, Influence of axial loads on CO2 and Cl− transport in concrete phases: Paste, mortar and ITZ, Constr. Build. Mater. 204 (2019) 875–883.

[104] S.A. Khan, S. Ahmed, S. Ali, F. Altaf, Advances in CO2 Capture Materials: From Strategies to CO2-Based Fertilizers for a Sustainable Future, Carbon Neutralization. 4 (2025) e70063.

[105] H. Huang, S. Zhang, Y. Wang, Y. Guo, C. Zhang, F. Qu, Cement-Based Electrochemical Systems for Structural Energy Storage: Progress and Prospects, Materials (Basel). 18 (2025) 3601.

[106] D.D.L. Chung, CARBON–CEMENT COMPOSITES, in: Fibers Compos., CRC Press, 2003: pp. 219–242.

[107] H.N. Yoon, D. Jang, T. Kil, H.K. Lee, Influence of various deterioration factors on the electrical properties of conductive cement paste, Constr. Build. Mater. 367 (2023) 130289.

[108] L. Bing, M. Ma, L. Liu, J. Wang, L. Niu, F. Xi, An investigation of the global uptake of CO 2 by lime from 1930 to 2020, Earth Syst. Sci. Data. 15 (2023) 2431–2444.

[109] C. Shao, Z. Liu, Z. Xu, B. Wang, J. Li, L. Liang, D. Wang, Study on the performance evolution and carbonation mechanism of natural hydraulic lime under different CO2 concentrations, Constr. Build. Mater. 481 (2025) 141619.

[110] X.D. Zhou, CO_2 uptake through carbonation of concrete using simulated and as-captured flue gas, (2005).

[111] N. Vidal-De la Peña, S. Grigoletto, D. Toye, L. Courard, G. Léonard, CO2 capture by mineral carbonation of construction and industrial wastes, in: Circ. Econ. Process. CO_2 Capture Util., Elsevier, 2024: pp. 163–185.

[112] L. Liu, Y. Wang, G. Liu, L. Chen, Investigation on carbon sequestration performance of cement slurry by sodium carbonate modified biochar, Constr. Build. Mater. 494 (2025) 143348.

[113] P. Paşabeyoğlu, Sustainable zeolite production via solar calcination of kaolin and halloysite: structural evolution, phase control, and CO_2 adsorption efficiency, (2025).

[114] M.F. Aufa, Analisis Pengaruh Variasi Komposisi Activated Carbon Dan Fly Ash Terhadap Kuat Tekan Dan Kemampuan Adsorpsi CO2 Bahan Komposit FA/GGBFS/Semen/AC, (2024).

[115] D. Cantador-Fernandez, J.I. Alvarez, I. Navarro-Blasco, J.R. Jiménez, J.M. Fernández-Rodríguez, Compatibility of CO2 adsorbents with cement-, lime-and cement-lime based materials. Innovations in carbon capture and utilization technologies, Chem. Eng. J. (2025) 164424.

[116] S.-H. Kang, Y.-H. Kwon, J. Moon, Quantitative analysis of CO2 uptake and mechanical properties of air lime-based materials, Energies. 12 (2019) 2903.

[117] C. Lawrie, A review of CO_2 capture adsorbents: Carbonate/oxide systems and aerogel synthesis, (2023).

[118] M. Finkbeiner, R. Tan, M. Reginald, Life cycle assessment (ISO 14040/44) as basis for environmental declarations and carbon footprint of products, in: ISO Tech. Comm. 207 Work. Norw., 2011.

[119] G. Habert, S.A. Miller, V.M. John, J.L. Provis, A. Favier, A. Horvath, K.L. Scrivener, Environmental impacts and decarbonization strategies in the cement and concrete industries, Nat. Rev. Earth Environ. 1 (2020) 559–573.

[120] L.K. Turner, F.G. Collins, Carbon dioxide equivalent (CO2-e) emissions: A comparison between geopolymer and OPC cement concrete, Constr. Build. Mater. 43 (2013) 125–130.

[121] D.M. Martinez, A. Horvath, P.J.M. Monteiro, Comparative environmental assessment of limestone calcined clay cements and typical blended cements, Environ. Res. Commun. 5 (2023) 55002.

[122] S.A. Miller, A. Horvath, P.J.M. Monteiro, Readily implementable techniques can cut annual CO2

emissions from the production of concrete by over 20%, Environ. Res. Lett. 11 (2016) 74029.

[123] J. Carvalho, L. Nascimento, M. Soares, N. Valério, A. Ribeiro, L. Faria, A. Silva, N. Pacheco, J. Araújo, C. Vilarinho, Life cycle assessment (LCA) of biochar production from a circular economy perspective, Processes. 10 (2022) 2684.

[124] K. Scrivener, F. Avet, F. Zunino, J. Ston, More sustainable constructions using limestone calcined clay cement (LC3), in: Proc. 5th Int. Conf. Sustain. Constr. Mater. Technol. SCMT, 2019: pp. 14–17.

[125] S.S. Berriel, A. Favier, E.R. Domínguez, I.R.S. Machado, U. Heierli, K. Scrivener, F.M. Hernández, G. Habert, Assessing the environmental and economic potential of Limestone Calcined Clay Cement in Cuba, J. Clean. Prod. 124 (2016) 361–369.

[126] H.Z. Ozek, Sustainability, biodegradability and life cycle analysis of wool, in: Wool Handb., Elsevier, 2024: pp. 401–440.

[127] A. Laveglia, N. Ukrainczyk, N. De Belie, E. Koenders, From quarry to carbon sink: process-based LCA modelling of lime-based construction materials for net-zero and carbon-negative transformation, Green Chem. 26 (2024) 6584–6600.

[128] L. Sambataro, LCA modelling of Cement and Lime-based Construction Materials Systems, (2024).

Declaration of interests

☒ The authors declare that they have no known competing financial interests or personal relationships that could have appeared to influence the work reported in this paper.

☐ The authors declare the following financial interests/personal relationships which may be considered as potential competing interests: